Summer 2017

Virtual Substrate Synthesis for Low-Cost High Efficiency III-V

Sean J. Babcock
Old Dominion University

VIRTUAL SUBSTRATE SYNTHESIS FOR LOW-COST HIGH EFFICIENCY III-V PHOTOVOLTAICS

by

Sean J. Babcock
B.S. August 2015, Old Dominion University

A Thesis Submitted to the Faculty of
Old Dominion University in Partial Fulfillment of the
Requirements for the Degree of

MASTER OF SCIENCE

ELECTRICAL AND COMPUTER ENGINEERING

OLD DOMINION UNIVERSITY
Aug 2017

Approved by:

_____
Christopher Bailey (Director)

_____
Sylvain Marsillac (Member)

_____
Gon Namkoong (Member)

ABSTRACT

VIRTUAL SUBSTRATE SYNTHESIS FOR LOW-COST HIGH EFFICIENCY III-V PHOTOVOLTAICS

Sean J. Babcock
Old Dominion University, 2017
Director: Dr. Christopher Bailey

The use of the low-cost thin-film vapor-liquid-solid (TF-VLS) method in the manufacturing of III-V solar cell substrates has the potential to provide a lightweight, flexible, and cheaper alternative to traditional III-V substrates typical of state-of-the-art power generation technology. The TF-VLS process has been shown to produce high optoelectronic quality polycrystalline InP on lightweight flexible metal foils. In this work, this novel method is applied to the growth of binary and ternary III-V materials which include: InP, InAs, and InGaP on Mo foils and/or sputtered Mo on Si wafers.

As a result of InP trials, powder XRD measurements have identified the presence of polycrystalline InP peaks and the absence of pure unbound In peaks, signifying full consumption of In by InP formation. Photoluminescence measurements show InP samples emit in close agreement to the InP bandgap of 1.34 eV and share similar FWHM values with single crystal InP, indicating the optical properties of the TF-VLS grown material is similar to that of single crystal InP. Cross-section SEM of InP grown on Mo/Si demonstrate crystal growth in a planar format without defects such as pinholes or voids throughout the InP layer. A series of studies were performed to investigate the effects of varying phosphorization parameters such as temperature and partial pressure of phosphorous gas. Temperature studies show that varying phosphorization temperatures do not seem to have a pronounced effect on crystallinity but they do have an effect on the optical quality of the material. For both studies, at two different partial pressures, the PL intensity for the InP grown at higher temperatures is greater than InP grown at lower temperatures, thereby indicating a temperature dependence on the optical quality of the material. Partial pressure studies revealed that samples phosphorized at lower pressures demonstrate greater PL intensities indicating higher radiative recombination efficiency and partial pressure dependence on the optical quality of the material.

The TF-VLS method was expanded to polycrystalline InAs growth with trials indicating multiple InAs XRD peaks but with a number of unidentified peaks. Photoluminesce of TF-VLS grown InGaP show five distinguishable peaks corresponding to bandgaps ranging from 1.28-1.65 eV, possibly indicating different phases of InGaP or materials other than the intended InGaP.

Initial In layer optimization efforts conclude that In sputtered at a low pressure (1 mTorr) show more surface coverage than at higher pressures. Electron beam studies show that surface morphology of the In layer becomes more planar and continuous with simultaneously increased deposition rate and layer thickness. Electron beam vs. RF sputtering comparison prove the former method to be vastly superior to the latter, validating electron beam deposition as the preferred In deposition method for the growth of high quality polycrystalline III-V materials. Collectively, these efforts aim to improve the novel TF-VLS growth process to provide low-cost substrates for next-generation III-V photovoltaic technology.

I dedicate this thesis to my very supportive and loving wife Alyssa Babcock and to my late mother, Eileen Bowler, who instilled in all of her children the drive to become successful at whatever it is we decide to do.

ACKNOWLEDGEMENTS

This work was supported by the National Science Foundation's SoLar Engineering Academic Program (SoLEAP, contract number 1355678). Without this funding it would have not been possible to pursue graduate school. I would like to acknowledge (in no particular order) three members of Old Dominion University's (ODU) Department of Electrical and Computer Engineering faculty who have been especially influential to my academic career thus far and my decision to pursue higher education and an eventual career in photovoltaic (PV) research.

My first hands-on exposure to PV research was under the instruction of Dr. Gon Namkoong while working on my electrical engineering senior design project. His guidance and lectures regarding PV physics was with an enthusiasm that effectively steered the course of my academic interest toward PV related research. There was no turning back as I completed a physics undergraduate thesis with his guidance as research adviser to the project. In my final undergraduate semester, Dr. Namkoong convinced me to pursue a M.S. degree with a focus in PV technology that will come into fruition upon acceptance of this thesis.

Since my junior year, Dr. Sylvain Marsillac has acted as an unoffical mentor to me as he would consistently take a special interest in my academic and research activities. The Microelectronic Materials and Processes course he regularly instructs was my first exposure to techniques used to design and fabricate semiconductors. His passion about the topic came through in his lectures as he would speak in great detail and clarity of the topics under discussion. The lab component to this course provided me with my first hands-on experience in semiconductor fabrication which proved instrumental to my understanding of the physics at work. I have since worked closely with Dr. Marsillac on various research endeavors which typically promote intellectually stimulating conversions about innovative ways to impact future PV technology.

As a student with an interest in pursuing an advanced degree in PV, Dr. Christopher Bailey took me under his wing during my final undergraduate semester to prepare me for graduate studies by providing exposure to graduate level PV research and technology. He has since employed me as his graduate student where I continue to learn from his expertise in leading-edge PV related experimental and theoretical physics. He educates his vast knowledge base with contagious enthusiasm and clarity

making it not just easy to understand the complicated subject matter but to become passionate about it yourself. Under his mentorship, I have gained the invaluable knowledge and experience required for the challenges of future academic and professional ventures. I owe the knowledge achieved during the research leading up to this thesis to Dr. Bailey as I remember the long hours spent engaged in conversations regarding theoretical physics, the latest experimental results, and the planning of new and exciting experimental pathways.

During my time at ODU, these professors have proved to be extraordinary mentors and educators with respect to academic, professional, and personal ambitions alike. Future students have the world to gain from this team of accomplished academics and photovoltaic scientists.

I extend additional acknowledgments to fellow graduate research colleagues Grace Rajan, Shankar Karki, and Tasnuva Ashrafee who showed me the ropes as a new graduate student and who continually engage me with interesting conversation and thought provoking ideas. I couldn't have learned from a better group.

Finally, I would like to extend a special thank you to my wife, Alyssa Babcock, and family for the continuous love and support throughout these academic endeavors.

NOMENCLATURE

PV	photovoltaic
PVD	physical vapor deposition
VPE	vapor phase epitaxy
MOCVD	metal-organic chemical vapor deposition
CVD	chemical vapor deposition
VLS	vapor-liquid-solid
TF-VLS	thin-film vapor-liquid-solid
SEM	scanning electron microscope
EDX (or EDS)	energy-dispersive X-ray spectroscopy
XRD	x-ray diffraction
PL	photoluminescence

TABLE OF CONTENTS

LIST OF TABLES

LIST OF FIGURES

CHAPTER 1

INTRODUCTION

1.1 ENERGY CONSUMPTION

Human energy consumption is not something that shows any signs of slowing. Access to affordable energy is what defines modern civilization and is considered a measurement for quality of life. Today's modern society has adapted to a high-energy consumption lifestyle where on-demand electricity is expected to be available at the flick of a switch to power amenities such as lighting, air conditioning, and electronics. Additionally, the advent of automobiles has provided a massive source of energy consumption as it has become typical for an average household to own and operate multiple vehicles. Data published by the U.S. Energy Information Administration (EIA) shows global energy consumption is on the rise. In 2014, the world consumed primary energy at a rate of 18 terawatts (TW) of which China, United States, Russia, and India collectively account for 51% of consumption [1]. Primary energy is defined as energy that has been harvested directly from natural resources which includes non-renewable sources such as fossil fuels and uranium and renewable sources such as solar, wind, tidal, biomass, and geothermal energy. EIA data projects primary energy consumption to increase to 27 TW by 2040 [2]. With the rate of energy consumption on the rise, non-renewable resource stockpiles will experience considerable strain.

Much of global energy consumption is derived from fossil fuels such as petroleum, coal, and natural gas. These energy sources are not only unsustainable due to their finite supply but they are known to emit harmful CO_2 gasses into the atmosphere as a byproduct of burning hydrocarbons, which if burned in the presence of oxygen will break H-C bonds resulting in carbon dioxide (CO_2) and water vapor (H_2O). Theses gasses along with methane (CH_4) are the greenhouse gasses that prevent heat from escaping into space, thereby acting as Earth's blanket allowing for life sustaining temperatures. The release of CO_2 that has been encapsulated by the Earth resulting from ancient plant and animal decomposition is in excess to the CO_2 released naturally by plant and animal respiration, volcanic eruption, and ocean-atmosphere exchange. As a consequence of the amount of fossil fuels needed to

feed humanity's insatiable appetite for energy, massive amounts of excess CO_2, once stored beneath Earth's surface for millions of years, is emitted into the atmosphere at a high rate allowing for the Earth to retain more heat than natural in a relatively short amount of time. The concentration of atmospheric CO_2 has increased more than 40% since pre-industrial times from approximately 280 parts per million by volume in the 18th century to over 400 ppmv in 2015 [3]. This has led to the environmental crisis know as global warming which is attributed to the rise of sea levels, an increase in stronger and more destructive storms, and changes in rainfall causing flooding, droughts, and heatwaves [4]. Not surprisingly, the same four nations that collectively account for 51% of global energy consumption are responsible for 55% of the 33 billion metric tons of 2014's CO_2 emissions [5]. Greenhouse gas emissions have been linked to an increase in Earth's average temperature which has risen by 0.8 °C over the past century and is projected to increase another 0.3 to 4.8 °C over the next century [3].

Fossil fuels certainly kick-started the industrial age and carried the modern world into globalization made possible through the availability of affordable transportation. However, diminishing energy supplies and environmental impact could simultaneously mature into global crises as world powers compete over remaining energy resources and climate change fallout displaces homes and communities. Advancements in renewable energy technology is a viable solution to provide relief from the burden of fossil fuel dependency. Photovoltaic (PV) technology is on the forefront of this effort. With the enormous amount of virtually limitless energy supplied to Earth's surface from the Sun there is an obvious interest in improving solar energy conversion technology. The amount of solar energy reaching Earth's surface annually is on the order of 10,000 times the current global energy consumption [4]. If just a small fraction of these photons could be harvested as energy the result could mean global energy security achievable in our lifetime and enjoyed for generations to come.

1.2 BRIEF PHOTOVOLTAIC HISTORY

In 1839, Alexandre Edmond Becquerel discovered the photoelectric effect while experimenting with platinum plates submerged in an electrolyte solution [6]. While measuring the current flow between two plates, he discovered that there was an increase in current flow when exposed to light. In 1873, Willoughby Smith and his assistant Joseph May, discovered that the resistance of selenium varied when exposed

to light [6]. This was the first observation of light causing electrons to be freed from their bound state and available as free charge carriers in semiconductor material. In 1876, William Grylls Adams and his student, Richard Evans Day discovered that an electrical current could be produced by exposing a selenium rod to illumination, thereby converting light into electricity without heat or moving parts [6]. In 1883, Charles Fritts built a small solar cell module (surface area of 30 cm^2) of selenium cells and recorded an efficiency of 1%. In 1905, Albert Einstein published "Concerning an Heuristic Point of View Toward the Emission and Transformation of Light." which introduced the idea that light contains packets of energy called quanta. In 1916, the Polish chemist Jan Czochralski invented crystal growth process that was named after him and still in use today. It wasn't until the 1950's when progress in photovolatics began to really accelerate. In 1950, William B. Shockley published "Holes and Electrons" which described the physics of the pn junction which laid the groundwork for semiconductor fundamentals. The first silicon solar cell, developed by Bell Labs, was fabricated with an area of 2 cm^2 and demonstrated an efficiency of 6% in 1954. As the efficiency was increased to 10 %, extremely high costs limited their use to specialized applications such as space satellites. In 1958, Vanguard I became the first satellite to use solar cells and subsequently powered one of its transmitters until 1964 [6]. In the 1960's, non-silicon solar cells such as GaAs was being used for space applications. The energy crisis of the 1970's heightened the interest in photovoltaic technology which allowed for an increase in funding for related projects. Since then, there have been major improvements in device efficiency as well as reduced costs as researchers find new and innovative ways to push the boundaries of photovoltaic technology. In the following section, a brief overview of this progress will be discussed.

1.2.1 OVERVIEW OF PROGRESS IN PV TECHNOLOGY

Fig. 1.1 shows the most recent solar cell efficiency chart generated and updated by the National Renewable Energy Laboratory (NREL) regularly throughout the year. The plot shows the best research cell efficiencies starting from 1976 to present for solar cell categories which include: multijuntion cells, single junction GaAs, crystalline Si, thin film technologies (CIGS, CdTe), and a group of emerging technologies such as organics and perovskite solar cells. Silicon, being one of the first technologies to emerge, has plateaued in performance over the years showing only minor

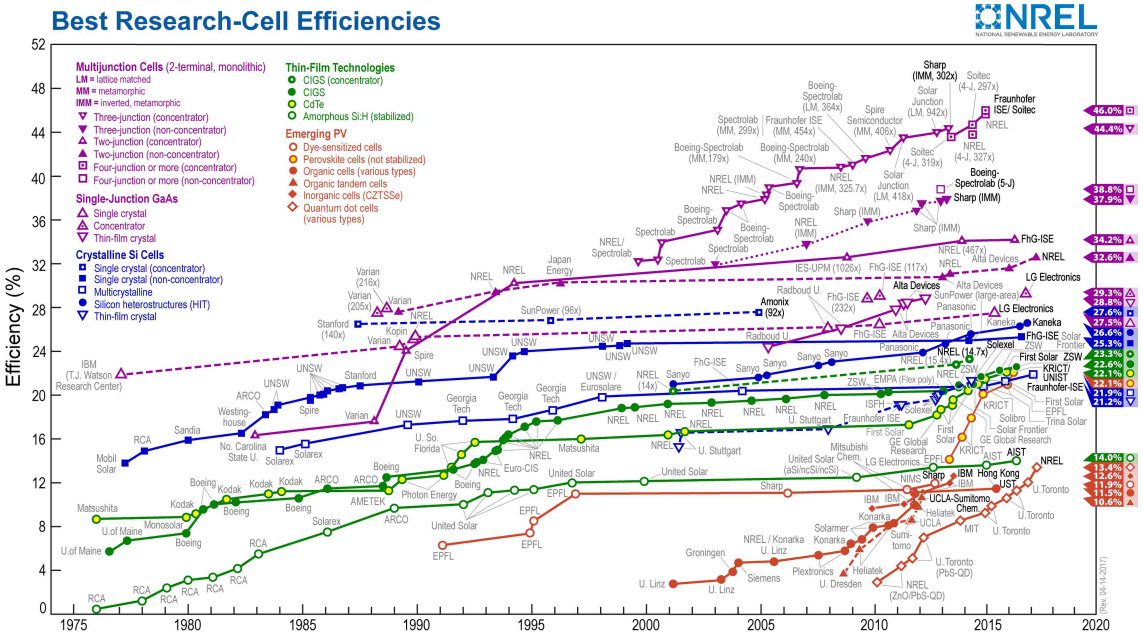

FIG. 1.1: Best research solar cell efficiencies from 1976 to 2017.

improvements during the past two decades. The current record for single crystal non-concentrator Si cells is 25.3%. What appears to be enjoying significant improvements are the multijunction and emerging PV groups. Multijuntion technology, currently at 46%, has demonstrated some of the highest efficiencies since their introduction in the late 1990's and still has one of the largest improvement rates on the chart signifying they will not plateau anytime soon. Exciting new technologies such as quantum dots (13.4%), organics (11.5%), and perovskites (22.1%) have relatively low efficiencies in comparison but share the same increasing rate of improvement as multijunction technologies. Efficiency isn't the only important factor when it comes to integrating PV technology into a society dominated by fossil fuels. Until PV power generation is cheaper than what is currently available, researchers will have to push the boundaries with cost reduction innovations in addition to efficiency improvement efforts. The following section will discuss what effects the latter in greater detail.

1.3 PHOTOVOLTAIC PHYSICS

1.3.1 SOLAR IRRADIANCE

Photovoltaic is a term used to describe photon to electron energy conversion via the photovoltaic effect using semiconductor materials. The transferred energy could then be used to provide electrical power for a wide array of electric/electronic devices. The photovoltaic effect begins with a photon that has traveled 93 million miles from the Sun to Earth's surface in just over 8 minutes to provide Earth with the energy required to sustain life. Each photon is defined by its energy (or wavelength) which can be determined using the relationship

$$E = \frac{hc}{\lambda}, \tag{1.1}$$

where E is the photon's energy, h is Plank's constant, c is the speed of light, and λ is the photon's wavelength (in SI units). Simplification of the equation results in the form

$$E(eV) = \frac{1240}{\lambda(nm)}, \tag{1.2}$$

which provides for convenient conversion from energy to/from wavelength using units commonly used in semiconductor mathematics: eV and nm. The Sun emits photons spanning a wide range of wavelengths from 250 to 4000 nm that appear white when observed collectively. The Sun's surface can reach up to 6000 K with a radiation spectrum closely resembling that of a black body and a power density proportional to distance from its surface which is 1300 W/m^2 at Earth's distance of 150x10^6 km. Fig. 1.2 illustrates that the solar radiation outside Earth's atmosphere differs slightly from the radiation seen from its surface due to absorption and scattering of photons of specific wavelengths by atmospheric particles such as H_2O, CO_2, and O_3 [7]. Additional factors such as dust particles, time of day/year and geographical location also play a roll in varying the solar radiation (and power density) seen on Earth's surface. To account for loss in power density at Earth's surface due to atmospheric power limiting effects, air mass calculations are used. Air mass is defined as the path length that light travels through the atmosphere to the surface of the Earth and is defined as

$$AM = \frac{1}{\cos(\theta)}, \tag{1.3}$$

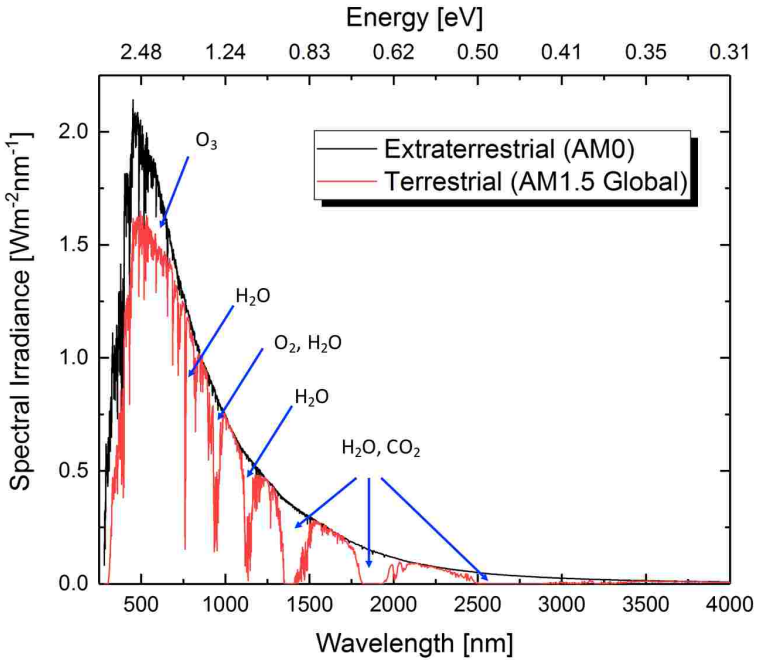

FIG. 1.2: Terrestrial (AM1.5 Global) and extraterrestrial (AM0) solar spectrum standardized for photovoltaic performance comparison with integrated power of 1000 W/m^2 and 1366.1 W/m^2, respectively.

where θ is the angle of the Sun's position with respect to its vertical (sun directly overhead). For example, when the Sun makes an angle of $\theta = 48.2$ degrees with respect to Earth's vertical, $AM = 1.5$. Because atmospheric effects widely vary the power density seen by Earth's surface due to time of day/year and geographic location and because solar cell efficiency is highly dependent on power density, the solar spectrum and power density was standardized so that photovoltaics can be compared fairly across academic and industry research groups internationally. The standardized spectrum for terrestrial and extraterrestrial solar spectrum are AM1.5 Global and AM0, respectively. The power density for AM1.5 and AM0 are 1000 W/m^2 and 1366.1 W/m^2, respectively. These solar spectrums and power densities are replicated using solar simulators for solar cell device efficiency testing.

1.3.2 SOLAR CELL DEVICE PHYSICS

Solar cells are made from semiconductor materials from either the group IV column from the periodic table, a combination of group III and V columns, or a combination of group II and VI columns such as Si, GaAs, and CdTe, respectively. A solar cell at its most basic consists of two layers of a semiconductor material (silicon for example) sandwiched together between metal contacts as illustrated by Fig. 1.3. The

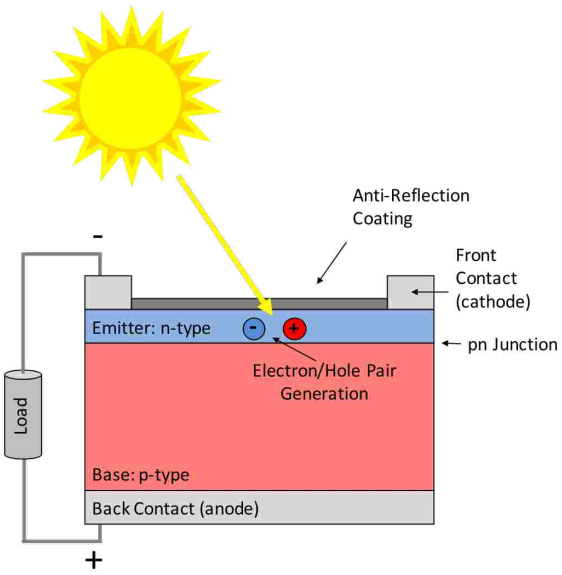

FIG. 1.3: Typical single junction solar cell device.

emitter layer is doped with extra electrons (n-type Si) while the base is doped with extra holes (p-type Si). Two common n-type and p-type dopants for silicon solar cells are phosphorous and boron, respectively. The dopant atoms replace silicon atoms making the material more negatively or positively charged depending on the dopant. For example, to make the emitter layer (n-type), silicon would need to be doped with extra electrons. To do this, an impurity is added that has more valance electrons per atom than silicon, which has four. Phosphorous has five valance electrons, one more than silicon and therefore is commonly used as a n-type dopant. When silicon is doped with phosphorous, phosphorous atoms replace silicon atoms in the lattice. Without the dopant (Fig. 1.4a), the silicon atoms are held together in the lattice via its four electrons that form eight covalent bonds with neighboring silicon atoms.

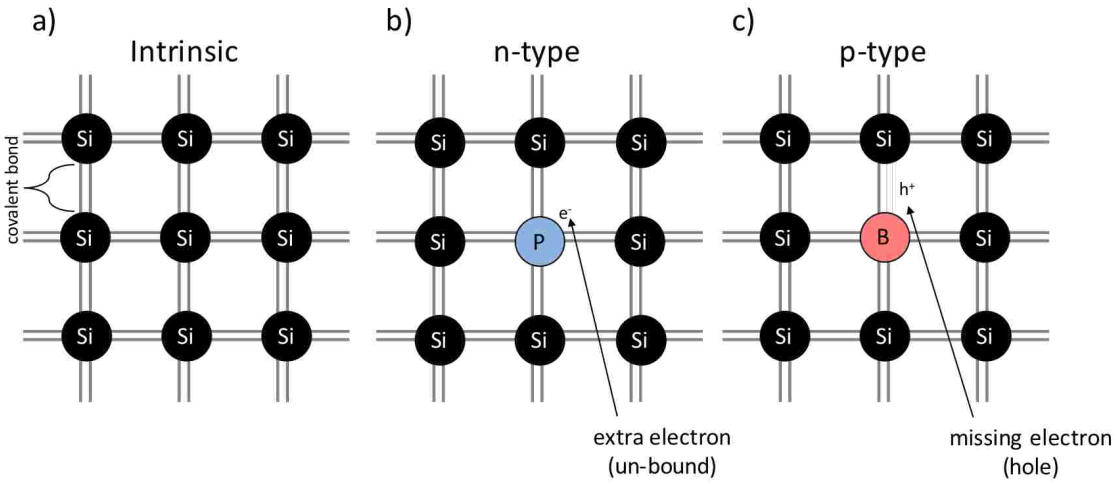

FIG. 1.4: Doped and undoped silicon lattice: a) intrinsic, b) n-type, c) p-type.

When the silicon is doped with phosphorous (Fig. 1.4b), phosphorous atoms replace the silicons atoms in the lattice thereby making the material electrically negative due to the extra electron. Conversely, when silicon is doped p-type, boron atoms replace silicon atoms making the material electrically positive due to the absence of an electron since boron has only 3 valance electrons. When the n-type and p-type materials are sandwiched together, the interface is know as a pn junction and is fundamental for all semiconductor and solar cell operations. The purpose of the junction is to spatially separate the electrons and holes to prevent them from recombining with each other before they can be collected for power generation. The spatial separation is a result of the electric field that exists at the pn junction. In the n-type material, electrons are the majority charge carrier and holes are the minority carrier. In the p-type material, holes are the majority charge carrier and electrons are the minority carrier. If a minority carrier gets too close to the pn junction, it will be swept to the other side by the electric field and become the majority carrier.

The basic process for photon to electron energy conversion can be broken into two main steps, 1) photon absorption and 2) charge collection by the positive and negative electrodes (anode/cathode). The former process begins with photons emitted from the sun striking the surface of the solar cell, illustrated by Fig. 1.3. Whether the photon is absorbed by or transmitted through the solar cell depends on the energy

of the photon and the bandgap of the semiconductor material. The bandgap is the minimum energy required to remove an electron from a bound state (valance band) to a free state where it can participate in conduction (conduction band). This is the minimum energy required for a photon with a particular energy to become absorbed. If a photon with an energy lower than the material's bandgap strikes the material, the photon will not be absorbed but will instead be transmitted through the material. A photon with an energy equal to or greater than the material's bandgap will be absorbed thereby transferring its energy to an electron which will use it to break free from its bound state in the valance shell to become a free electron. When this happens, the electron is said to be excited from the valance band to the conduction band. A photon that has an energy exactly matching the bandgap is excited to exactly the conduction band edge. A photon with energy exceeding the bandgap will also be absorbed but will excite to an energy level greater than the conduction band edge. In other words, the electron will have an energy greater than the minimum required for conduction. The excess energy is dissipated as heat to other atoms in the lattice as the electron relaxes to the conduction band edge. This dissipated energy is considered lost and does not contribute to power generation. The process of exciting an electron to the conduction band is not exclusive to the absorption of photons. The presence of heat, another form of energy, can also excite electron provided the energy is greater or equal to the material's bandgap. At room temperature, the small amount of thermally generated free electrons and holes moving about the material is called intrinsic carrier concentration and is related to solar cell efficiency.

The second process that must take place for power generation is charge collection. Following electron excitation, both charge carriers (electron and hole) are free to move about in the material. A hole is defined as the positive charge left behind in the absence of an electron. Therefore, a hole is where an electron used to be. It's easy to think about how an electron can move through a material because it is a physical object that takes up space and has mass. Holes, on the other-hand, are not physical objects but can still move around as if they are. The movement of holes occurs when they become occupied by other electrons. Once an electron moves into a hole, another hole is created where that electron used to be, therefore holes can move around indirectly as electrons work to fill them. For this reason, holes are known to move at a slower rate than electrons since their movements are constrained by the lattice whereas electrons can move through physical space the same way a ball is

free to roll about on a flat surface. The flow of current occurs when the n-type and p-type materials are connected together using a conductor (wire) which is illustrated in Fig. 1.3. When light is absorbed by the n-type material, an electron/hole pair is created. The majority carrier electron is then free to travel through the cathode and out through the wire. The minority carrier hole will be swept across the pn junction due to its electric field. The electron will then travel to the anode via wire and recombine with free holes, thereby completing the circuit. Applying voltages and measuring the current at each voltage will produce a current density (J) vs. applied voltage (V) curve which is used to extrapolate information about the device such as open-circuit voltage V_{oc}, short circuit current J_{sc}, fill factor FF, and power conversion efficiency PCE.

1.3.3 SOLAR CELL DEVICE EFFICIENCY

Fig. 1.5 illustrates a typical JV curve and its corresponding performance parameters as a result of Eq. 1.4 used to model measurements performed while the solar cell is under illumination. For

$$J = J_0 \left[\exp\left(\frac{qV}{nkT}\right) - 1 \right] - J_L, \tag{1.4}$$

J is the total current achieved as a result of applied voltage V at room temperature T, J_0 is the dark saturation current, J_L is the photo generated current, and n is the diode ideality factor. With the J_L term omitted, Eq. 1.4 reduces to the diode equation. In Fig. 1.5, the short circuit current (J_{sc}) can be observed at the location where $V = 0$. This is analogous to shorting the emitter (n-type) and base (p-type) together without a load attached (see Fig. 1.3). The JV curve represents the superposition of dark current (diode) and light-generated current. When JV measurements are performed in the dark, the curve would be shifted up by the J_{sc} value. Therefore, $J_{sc} = J_L$ and is the measure of light generated current.

The open circuit voltage (V_{oc}) is the maximum possible voltage value that can be achieved by the solar cell and occurs when the current is zero. This is analogous to opening the circuit between the emitter and base (Fig. 1.3). The equation for V_{oc} can be determined by setting the total current J in Eq. 1.4 equal to zero and solving for V.

$$V_{oc} = \frac{nkT}{q} \ln\left(\frac{J_L}{J_0} + 1\right), \tag{1.5}$$

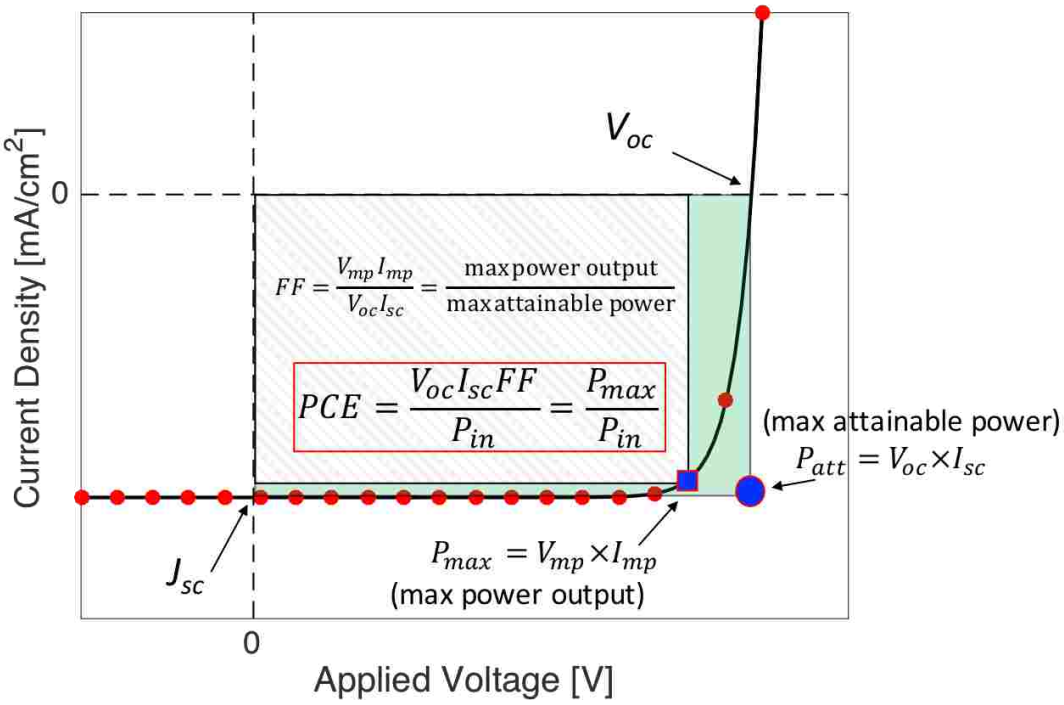

FIG. 1.5: Solar cell JV characteristics.

Together, the J_{sc} and V_{oc} multiply to result in the maximum attainable power P_{att}, which could never be obtained in practice due to the non-ideal nature of semiconductors. However, the maximum power output P_{max} is the largest value achieved after multiplying all corresponding current and voltage values from the measurements. The ratio between the maximum power output and maximum attainable power is called the fill factor FF,

$$FF = \frac{V_{mp}I_{mp}}{V_{oc}I_{sc}} = \frac{P_{max}}{P_{att}}, \tag{1.6}$$

shown by the grey cross-hatched box under the JV curve in Fig. 1.5. The fill factor is a measure of the "squarness" of the JV curve and represents the a square with the largest possible area that can be fit inside the JV curve [7]. The fill factor is used to determine the power conversion efficiency

$$PCE = \frac{V_{oc}I_{sc}FF}{P_{in}} = \frac{P_{max}}{P_{in}}, \tag{1.7}$$

where P_{in}, the power density due to sunlight seen by the solar cell, is determined

by calculating the area under the AM1.5 solar spectrum shown in Fig. 1.2 which is 1000 W/m^2 or 100 mW/cm^2. PCE is the overall device efficiency that takes into account all photon generation and electron/hole recombination processes and is the value that is used to compare solar cells from research groups from around the world.

1.4 MOTIVATION

Today's terrestrial photovoltaic market is dominated by silicon based devices due to the element's abundance in nature (second only to oxygen in Earth's crust). However, the efficiency of silicon technology has plateaued during the past decade with an efficiency improvement of only 2.7% (1997: 24% , 2017: 26.7%) for terrestrial cells measured under the global AM 1.5 spectrum [8, 9]. Solar arrays typical of today's space missions benefit from the high efficiency and performance characteristics of III-V photovoltaics, but at a much higher cost compared to silicon. A III-V multijunction device currently holds the world record cell efficiency of 46% under the direct AM 1.5 spectrum at 508 sun illumination using the ternary and quaternary materials GaInP/GaAs; GaInAsP/GaInAs [9].

For the terrestrial solar cell market to break away from silicon technology and take advantage of high-efficiency devices, innovative growth methods must be implemented to combat the primary cost factor influencing the III-V device, expensive epitaxy growth processes. The work discussed here aims to replace expensive epitaxially grown substrates currently used to grow III-V devices with a low-cost, lightweight, flexible alternative using a modified version of the vapor-liquid-solid method traditionally used to grow nanowires to grow polycrystalline thin-film III-V materials. This thin-film adaptation was first introduced by Kapadia et al. in 2013 who demonstrated the growth of high optoelectronic quality polycrystalline InP on Mo foil with ultra-large grain size up to 100 µm, electron mobilities as high as 500 cm^2/V-s, minority lifetimes as long as 2.5 ns, and the potential for an open circuit voltage of 930 mV determined indirectly via photoluminescence efficiency measurements [10].

To analyze cost influencing factors on III-V solar cells the National Renewable Energy Laboratory (NREL) published a study in 2014 on III-V photovoltaic manufacturing costs which broke down the cost (in $/W) of each layer in a single-junction GaAs device into material, labor and maintenance, utility, and depreciation costs assuming 25% cell efficiency, precursor utilizations of 30% for the III- source and

20% for the V- source, 15 µm/hr GaAs growth rate, and 70% effective cell yield [11]. The study showed that the substrate layer accounted for 63% ($6.70/W) of overall device costs assuming 20 substrate reuses via epitaxially lift-off and $150 for a new 6 in diameter GaAs wafer cut into pseudo-squares (27% area loss) with area of 133 cm^2 ($1.13/$cm^2$). In comparison, the MOVPE growth of the GaAs base layer accounted for only 25% and the emitter layer was <1% of device costs. A scenario closer to what has been experimentally achieved, 5 reuses increases the substrate cost to $16/W and its cost impact from 63% to 80% [11]. For these reasons, the focus of this work is on low-cost substrate synthesis processes aimed to reduce overall III-V device costs.

In addition to cost reduction, this research aims to use the TF-VLS technique to target materials of specific lattice constants. Currently, commercially available substrates are limited to III-V binary materials. Multijunction PV architectures could benefit from PV substrates with alternative lattice constants not currently commercially available. This could be used in PV technology to target specific solar spectrums that vary geographically on Earth and in space. For example, solar cells deployed to the Mars surface would experience a solar spectrum different from that of AM0 due to the effects of atmospheric dust filtering solar radiation [12]. A solar array could be equipped with devices with bandgaps that are optimized to absorb solar radiation specific to an environment. TF-VLS technology could also be used to grow lattice matched devices in the effort to push the boundaries of efficiency. For example, device modeling has identified a 5.8 Å lattice matched multijunction device to exceed 51% efficiency under 100-sun illumination using select III-V ternary and quaternary materials (InGaAs, InGaAsP, and InAlAs) to target bandgaps of 0.94, 1.39, and 1.93 eV, respectively, to optimize solar spectrum absorption [13].

Efficiency prediction models and simulation software are used (developed by Zachary Bittner from Rochester Institute of Technology) to provide a pathway to achieving TF-VLS grown substrates. Fig.1.6 illustrates initial simulations developed for device efficiency vs. grain interface recombination velocity and grain size. This consists of a minority carrier collection model based on the drift-diffusion equations modified to take into account the effects which polycrystalline grain size have on minority carrier diffusion length. For this device, a 250 nm n-InP emitter and 1500 nm p-InP base are used. As shown in Fig. 1.6, with this preliminary model, and the use of InP material, 22% efficiency is achievable with sub-mm crystal grains (given

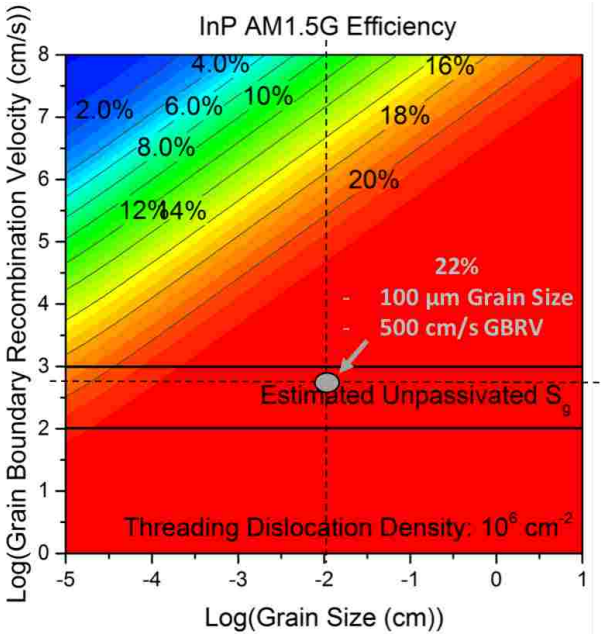

FIG. 1.6: Detailed balance-calculated efficiency contours as a function of grain size and boundary recombination velocity.

high intra-grain carrier lifetimes) and low unpassivated surface recombination velocity typical of p-type InP [14]. It should be noted that efficiency has been calculated up to 10 cm grain sizes, yet the largest grains attained using the TF-VLS growth method were 100 µm at maximum. This gives a target for reasonable efficiency values using polycrystalline material of this binary alloy, prior to materials optimization, but also a future expectation for the development of the high performance single junction devices needed to pursue the multijunction architecture.

Therefore, in order to achieve lattice-tuned III-V materials as a template for the epitaxy growth of solar cells at a reduction in cost compared to epitaxially grown substrates, this work employs the TF-VLS method to grow polycrystalline thin-film InP, InAs, and InGaP on lightweight flexible metal foils.

1.5 METHODOLOGY

The methodology to achieve low-cost lattice-tuned III-V binary and ternary materials as photovoltaic substrates begins first by repeating the efforts of Kapadia et al. by employing the novel TF-VLS method to the growth of polycrystalline InP on inexpensive flexible Mo foils. InP was chosen as a prototypical model by Kapadia et al. because it demonstrates promising characteristics as a thin-film polycrystalline material for optoelectronics due to its near-optimal bandgap (1.34 eV) for a single junction device and its low surface recombination velocity (500 cm/s) [10]. These efforts are then expanded on to include InP growth on sputtered Mo on a Si wafers. The benefits of using a rigid wafer in place of flexible foils include the ability to obtain cross-section SEM of the layers more easily, more uniform heat transfer due to better contact with the susceptor during phosphorization, and increased compatibility with existing semiconductor technology due to standardized wafer shape and sizes. Upon successful TF-VLS growth of InP, this works further expands to the growth of InAs and InGaP to provide a pathway for the growth of a wide array of binary and ternary III-V materials.

CHAPTER 2

EXPERIMENTAL

The work described in this thesis employed a variety of physical vapor deposition (PVD) and chemical vapor deposition (CVD) processes for the growth of polycrystalline InP, InAs, and InGaP which included magnetron sputtering, thermal evaporation, electron beam evaporation, and the use of a metal organic chemical vapour deposition (MOCVD) system for the TF-VLS processes. To characterize the resulting materials, a number of techniques were employed including scanning electron microscopy (SEM), energy-dispersive X-ray spectroscopy (EDX), x-ray diffraction (XRD), and steady state photoluminescence (PL). These crystal growth and characterization processes are described in detail in the following sections.

2.1 SPUTTERING

The sputtering equipment used in the experiments related to this thesis include the AJA International Orion-8 (Fig. 2.1a) and ATC-2030 (Fig. 2.1b) series magnetron sputtering systems. This equipment was used in the deposition of In and Mo on Mo foil and Si wafer surfaces. Prior to material deposition, the sputtering system chamber was evacuated of air to a vacuum on the order of 10^{-7} Torr. The chamber pressure must be low enough so that the mean-free-path (the average distance traveled by a gas molecule or other particle before colliding with other particles) is greater than the distance between the source material and the substrate [15]. Then Ar gas was introduced into the chamber and power applied to the sputtering guns to allow for the deposition of the materials onto the substrate.

Sputtering is a PVD process where a negative bias is applied to the target (source material such as: In, Mo, Al, Si, SiO_2, etc.) which is used to accelerate electrons into neutral gas atoms (such as Ar). If the accelerating electron's energy (from momentum) is large enough, it will knock free a valance electron from the Ar atom, thereby ionizing it. This now positively charged Ar atom is attracted to the negatively charged target (source material). When the accelerated Ar atom impacts the target, source material atoms become dislodged and travels in a straight path until it is

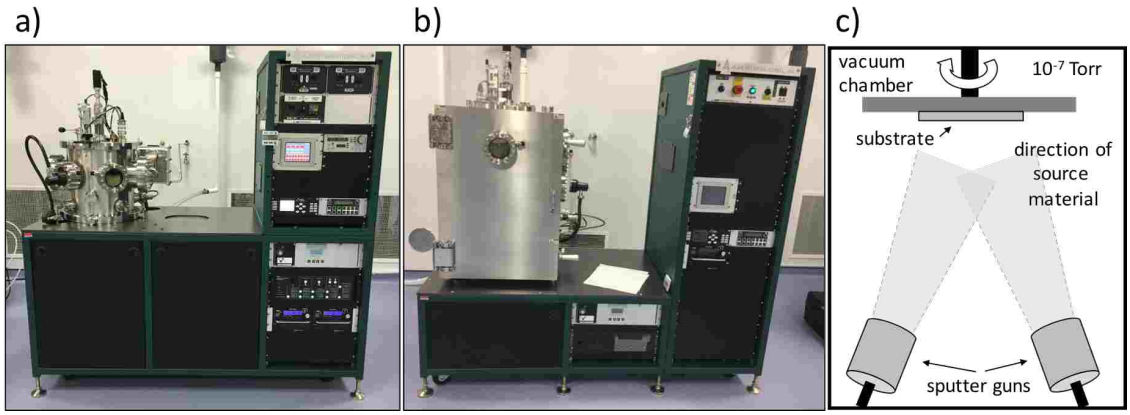

FIG. 2.1: AJA International magnetron sputtering deposition systems: a) Orion-8, b) ATC-2030, c) sputtering schematic.

obstructed by the either the intended substrate, the walls of the chamber, or anything else within the target material's line-of-sight. An illustration of the configuration is show in Fig. 2.1c. In addition to source material becoming dislodged upon Ar ion impact, electrons also become ejected and accelerated (due to targets negative bias) from the target and are free to collide with and ionize additional neutral Ar atoms. In addition to Ar atoms losing electrons and becoming ionized, they can also gain electrons via collisions with free electrons. The energy gained by the Ar atom in this process is emitted in the form of photons and is the source of the characteristic light that can be observed being emitted from the sputtering gun during deposition. Due to Ar ion/electron recombination, the electrons ejected from the source material upon Ar ion bombardment is critical in supplying the environment with new electrons to ionize neutral Ar atoms. Without these new electrons, the system will eventually run out of free electrons to ionize Ar atoms which will then cease to accelerate, impact, and dislodge source material, thereby shutting down the sputtering process. To make Ar ionization more efficient, magnetron sputtering was developed. This technology uses a magnetic field located at the negative electrode (target material) to capture and contain the free electrons directly above the target. This prevents the substrate from being bombarded by electrons, creating unwanted heat, and increases the probability of Ar ionization by an order of magnitude thereby increasing target material loss and therefore deposition rate [15]. The use of RF (radio frequency)

power alternates the bias at the target to prevent positive charged ion buildup when using dielectric materials.

2.2 THERMAL EVAPORATION

Thermal evaporation is one of the simplest PVD processes and was used in this work for the co-evaporation of In and Ga. For this setup, shown by Fig. 2.2, the chamber was evacuated of air to a vacuum on the order of 10^{-7} Torr. The chamber pressure must be low enough so that the mean-free-path is greater than the distance between the source material and the substrate [15]. Inside the chamber In and Ga pellets are contained by individual crucibles which are wrapped in metal coils. When an electric current is applied to the coils, they become heated due to resistance. When the material in the crucible heats past its melting point, it begins to evaporate into the chamber and will collect onto the nearby rotating substrate. The electric current is used to vary the crucible's heat which controls the material's deposition rate. To increase or decrease the deposition rate, the current is increased or decreased, respectively.

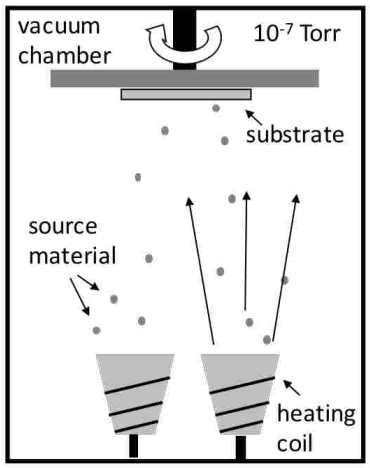

FIG. 2.2: Thermal evaporation chamber illustration.

2.3 ELECTRON BEAM EVAPORATION

For the deposition of In on Mo foils, a Kurt J. Lesker PVD 75 electron evaporation system was used. Electron beam evaporation (Fig. 2.3) is a PVD process that uses

a magnetic field to direct a beam of electrons (generated via thermionic emission) to heat up the source material to evaporation temperatures. For the work related to this thesis, electron beam evaporation was used to deposit a thin-film of In on Mo foil substrates. In pellets were placed inside the water-cooled holder and the chamber evacuated to a pressure on the order of 10^{-7} Torr. As with all evaporation processes, the chamber pressure must be low enough so that the mean-free-path is greater than the distance between the source material and the substrate [15]. With the electron

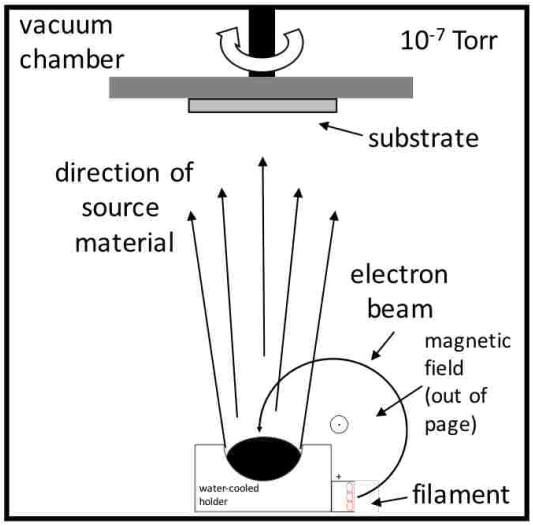

FIG. 2.3: Electron beam evaporation.

beam turned on and centered on the source material, an additional electromagnetic coil is used to "sweep" the beam around the source material for even heating. When the material is hot enough to evaporate, it then travels in a straight path until it reaches the rotating substrate (and surrounding area) resulting in a thin film of the source material on the substrate via deposition.

2.4 METAL-ORGANIC CHEMICAL VAPOR DEPOSITION

Metal-Organic Chemical Vapour Deposition (MOCVD) is a vapor-phase epitaxy (VPE) process where a single crystal substrate is used as a template for the growth of additional single crystal materials (or epitaxy film) such as the heteroeptitaxial growth of III-V and II-VI compounds [15]. For the work related to this thesis, a laminar flow quartz tube style MOCVD reactor (shown by Fig. 2.4) was used in the

phosphorization of In using PH_3 as the precursor. MOCVD systems are typically

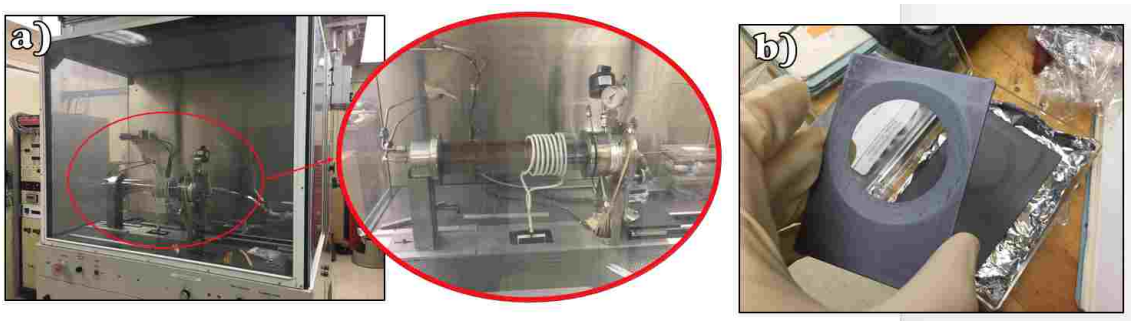

FIG. 2.4: a) Laminar flow quartz tube style MOCVD reactor located at the NASA Glenn Research Center, b) graphite sample susceptor.

reserved for the growth of single crystal materials, however, this work employs the equipment for the growth of polycrystalline InP. The difference is, for the single crystal growth of InP, a single crystal InP wafer would be used in conjunction with PH_3 and TMIn precursors [16]. The precursors would be simultaneously introduced into the chamber to form single crystal InP growth on InP substrates. For this work, a polycrystalline In/Mo(foil) substrate is used and only PH_3 is flowed through the chamber for polycrystalline InP growth. This InP/Mo(foil) stack would subsequently be used (in future work) for the MOCVD growth of InP solar cell layers. It should be noted that the use of an MOCVD for this work is not necessary. It has been shown, and will be discussed in greater detail in the next few sections, that polycrystalline InP can be grown as described above inside of a furnace, without the use of a MOCVD reactor.

2.5 VAPOR-LIQUID-SOLID NANOWIRE GROWTH

The vapor-liquid-solid method was first introduced in 1964 for the single crystal growth of silicon nanowires [17]. This method began with the deposition of gold on a Si wafer via sputtering or thermal evaporation (Fig. 2.5a). The resulting structure is then thermally annealed higher than the Au-Si eutectic point. The Au-Si alloy has a melting temperature lower than Au or Si independently causing the interface to melt while the Au and Si remain solid (Fig. 2.5b). Si gas is then introduced into the system and diffuses through the Au drop. The Si eventually diffuses through the Au until it reaches the Au/Si interface where the alloy is. The alloy eventually becomes

saturated with Si and the excess Si then bonds with the pure Si under the alloy and solidifies. As this process continues, the wire geometry continues to grow forming what is now know as a nanowire (Fig. 2.5c). This method has been shown to work for a variety of materials and is now an integral fabrication method for nanostructures.

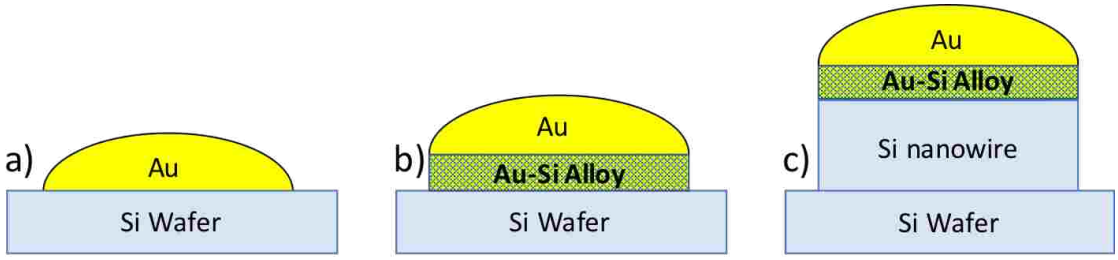

FIG. 2.5: VLS growth of silicon nanowires.

2.6 TF-VLS GROWN InP ON Mo FOIL

The TF-VLS-based polycrystalline InP growth process as described by Kapadia et al. (shown by Fig. 2.6) begins by depositing a layer of In (0.2 - 2 µm) and $Si0_2$

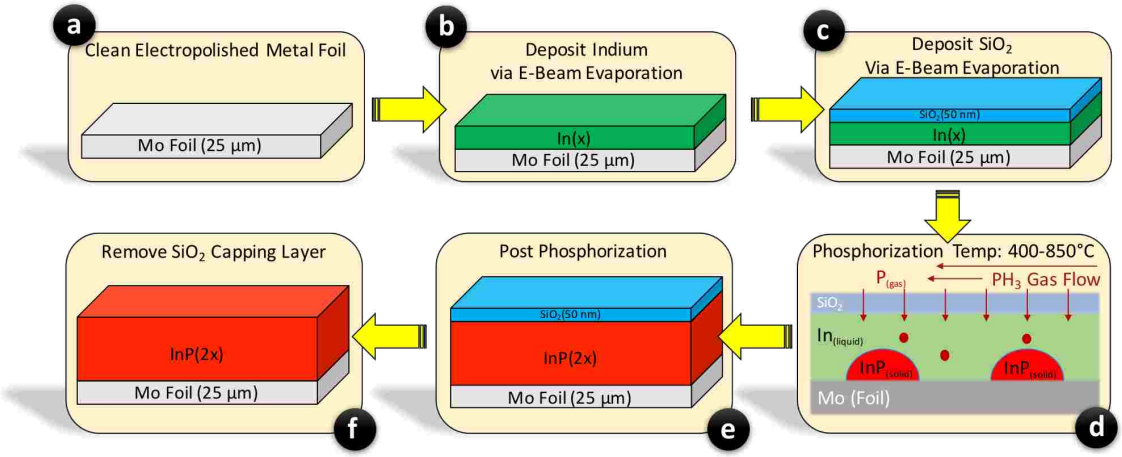

FIG. 2.6: Thin-film vapor-liquid-solid process steps.

(50nm) at room temperature on electropolished Mo foil (25 µm) via electron beam evaporation deposition method (Fig. 2.6a,b,c). The resulting stack is then placed into a heated furnace at temperatures ranging from 400-850°C (Fig. 2.6d), which

is well above the melting temperature of indium (157°C). Phosphine (PH_3) gas is then flowed through the chamber for tens of minutes. Phosphorous atoms then disassociate from the hydrogen and diffuse through the SiO_2 capping layer. The purpose of the SiO_2 capping layer is to maintain the planar geometry of the liquid indium by preventing it from dewetting during phosphorization. The phosphorous atoms then diffuse through the liquid indium to the indium/molybdenum interface which allows for the precipitation of solid InP crystals (melting temperature of InP: 1062°C). As this process continues, the InP nuclei continue to grow until all indium has been consumed by the formation of InP and the crystals converge into each other resulting in a continuous film of polycrystalline InP roughly double the thickness of the initial indium layer (Fig. 2.6e). The SiO_2 is then removed via hydrofluoric acid etch allowing for the epitaxy growth of subsequent solar cell layers (Fig. 2.6f).

The process described by this thesis (illustrated by Fig. 2.7) differs in several ways compared to the aforementioned steps introduced by Kapadia et al. First, the SiO_2 capping layer has been omitted to simplify the experiment by allowing for the investigation of In phosphorization in a more direct manner and to provide for a comprehensive baseline for future experiments which will incorporate the layer. Second, (Fig. 2.7b) RF magnetron sputtering was used for the deposition of indium in

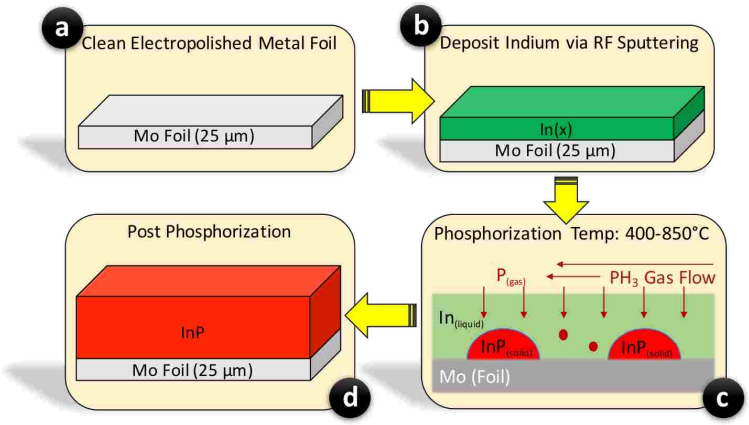

FIG. 2.7: Thin-film vapor-liquid-solid process steps without SiO_2 capping layer.

place of electron beam evaporation in an effort to investigate the effects of alternative deposition methods on the initial In layer. Finally, instead of a furnace, the In/Mo stack is placed in a graphite sample susceptor in a laminar flow quartz tube style

MOCVD reactor (Fig. 2.4) to allow for the phosphorization of In to InP (Fig. 2.7c). Without the SiO_2 layer to prevent the liquid In from dewetting, the resulting InP layer (Fig. 2.7d) is not expected to remain in a planar format compared to the initial In layer and therefore its thickness will not be uniform.

2.7 TF-VLS GROWN InP ON Mo/Si

In addition to the TF-VLS growth of InP on Mo foil, this work features InP growth on Mo that has been deposited on silicon wafers via RF sputtering (Fig. 2.8). The process steps are identical to the steps shown in Fig. 2.7 but a Mo/Si

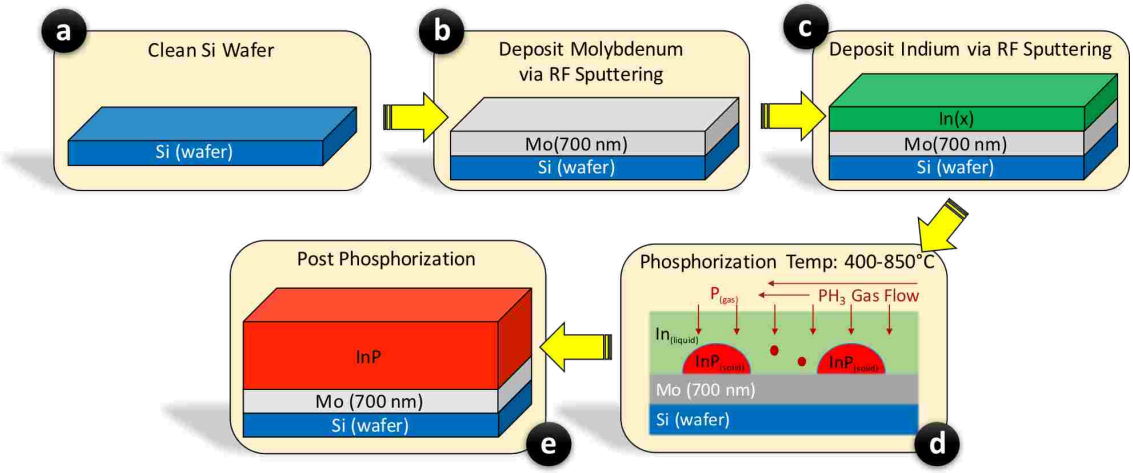

FIG. 2.8: Thin-film vapor-liquid-solid InP growth on Mo sputtered on an Si wafer.

stack is used in place of the Mo foil shown in Fig. 2.7a. There are a few reasons for the use of Si wafers. First, the experiment was designed to investigate if TF-VLS growth of InP could be repeated on sputtered Mo. Second, the rigid wafer allows for more uniform heat transfer during phosphorization compared to Mo foil due to the foil's non-uniform contact with the susceptor. Third, the rigidity of the Si wafer also allows for simplified cross-section SEM sample prep compared with Mo foil. Finally, compared to foil, silicon wafers are more compatible with existing semiconductor technology such as epitaxy growth and characterization equipment. All this, while keeping within the low-cost initiative as with the Mo foil.

2.8 TF-VLS GROWN InAs ON Mo FOIL

In addition to the growth of polycrystalline InP, this work expands the TF-VLS technique to the growth of the InAs binary. Using the same process steps and initial In/Mo(foil) stack described in Fig. 2.7, arsine was flowed through the chamber in place of phosphine.

2.9 TF-VLS GROWN InGaP ON Mo FOIL

This work further expanded the TF-VLS technique to the growth of the ternary InGaP. This process began with a 1:1 ratio of In and Ga deposited via co-evaporation at a rate of 1 Å/s and chamber pressure of 1 µTorr, thereby introducing both group-III materials simultaneously resulting in a 400 nm layer of $In_{0.5}$ $Ga_{0.5}$ alloy. Phosphorization occurred at 750°C with all other conditions identical as previously described for InP growth (Fig.2.7).

2.10 CHARACTERIZATION

In this work, techniques such as scanning electron microscopy (SEM), energy-dispersive X-ray spectroscopy (EDX), x-ray diffraction (XRD), and steady state photoluminescence (PL) were used for purposes of material characterization to determine planar and cross-section morphology, crystal structure, elemental information, and optical quality of InP, InAs, and InGaP. The following sections will go into detail about each technique.

2.10.1 SCANNING ELECTRON MICROSCOPE

For this work, a JEOL model 6060LV was used for the SEM imaging of III-V thin-film materials to analyze surface and cross-section morphology. Additionally, the JEOL model was equipped with EDX which was used for elemental spatial mapping of material surfaces. SEM technology works by using electrons to indirectly observe objects. This differs from an optical microscope which directly observes objects using photons. The need for SEM arose when it was necessary to view objects smaller than the wavelengths of visible light (700-900 nm). Basic SEM components include: vacuum chamber, thermionic electron gun, anode, magnetic lenses, scanning coil, backscatter electron detector, secondary electron detector, x-ray detector, and specimen stage. The process of SEM imaging begins by loading samples into and

evacuating the chamber to a vacuum on the order of 10^{-7} Torr. The electron gun supplies a high voltage (kV) to a filament that ejects electrons when heated. The electrons are then accelerated toward a positively charged anode and through a series of lenses that use electromagnetic force to focus them into a tight beam. This is similar to glass lenses used to focus light in an optical microscope. The specimen holder is also positively charged which helps the electrons maintain their path toward the specimen. When the electrons from the beam (called primary electrons) reach the specimen, they either become reflected (backscattered electron), dislodge an electron from the specimen (secondary electron), or become absorbed while emitting an x-ray photon in the process. The SEM uses detectors for each one of these processes. The backscattered and secondary electrons are used for electron imaging while the x-ray detector is used for energy-dispersive x-ray spectroscopy to determine elemental information about the specimen. The x-ray detector can also be used in conjunction with imaging to provide elemental mapping such as the one shown by Fig. 3.2. This process of bombarding the specimen with electrons and detection continues as the electron beam scans the surface of the specimen providing imaging based on the type of electron that is seen by the detectors. For example, if a surface is really smooth, more backscattered electrons will be detected. If the surface has ridges or grooves, more secondary electrons might be detected. All of this information is processed using digital electronics and software to provide an SEM image through indirect observation of the specimen being investigated.

2.10.2 X-RAY DIFFRACTION

For much of this work, the Rigaku Miniflex II benchtop XRD instrument and the International Centre for Diffraction Data (ICDD) database was used to verify the formation of III-V binary and ternary materials and to determine In consumption as a result of the TF-VLS process. X-ray diffraction is a non-destructive method of obtaining structural information and phase identification of crystalline materials. The fundamental operation of any diffractometer requires an x-ray source, sample holder, and x-ray detector. X-rays are used because their wavelength is on the same order of magnitude as crystal lattice spacing. The x-ray is generated using cathode ray tube technology which starts by heating a filament for the production of electrons which are then accelerated toward a target material (typically Cu). Electrons with sufficient energy then knock free electrons from the core shell of Cu atoms, thereby

emitting an x-ray spectrum in the process. Using a crystal monochromator, x-ray radiation is then filtered into monochromatic x-rays singling out only Kα radiation ($\lambda = 1.5418$ Å for CuKα) while filtering out Kβ radiation [18]. The resulting beam of x-rays is then directed at the sample material under investigation. Fig. 2.9 shows two incident x-rays (ray 1, ray 2) striking a material and then scattering (or reflecting) from the plane of crystal lattice material. Upon impact, some of the waves have to

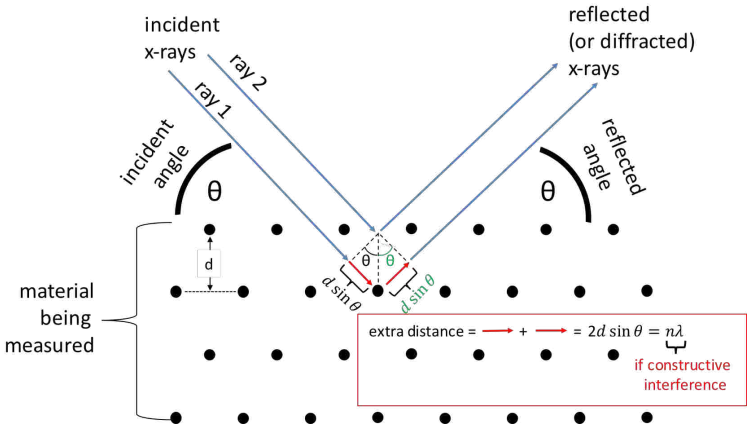

FIG. 2.9: Bragg's law for x-ray diffraction.

travel a longer distance than others. For example, ray 1 has a longer path to travel than ray 2. This extra path is denoted by the red arrows in the image. It is shown by the geometry of the diagram that the length of each red arrow is equal to $d\sin(\theta)$. Therefore, total extra path distance that ray 1 must travel is $2d\sin(\theta)$. If the extra distance happens to be an integer multiple of the x-ray's wavelength, then the waves are said to be in phase and constructively interfering with each other. When this happens, Bragg's Law is satisfied which is defined as

$$n\lambda = 2d\sin\theta, \tag{2.1}$$

where n is the order of reflection (positive integer), λ is the wavelength of the x-ray source ($\lambda = 1.5418$ Å for CuKα), d is the interplanar spacing, θ is the angle of incidence (or Bragg's angle) [18]. For powder XRD measurements, λ and θ are known values. A lot of crystal information can be extrapolated using Bragg's Law. For example, if the geometry of the crystal is known (such Miller indices hkl) d can be calculated using Bragg's law to obtain the material's lattice constant a using the

relationship

$$d = \frac{a}{\sqrt{h^2 + k^2 + l^2}}, \tag{2.2}$$

If Bragg's Law is satisfied and the x-rays have constructive interference then diffracted beam is measured by the detector which converts the x-rays into pulses of electric current. Electronic equipment is then used to count the pulses per unit time which is directly proportional to the intensity of the diffracted beam of x-rays [18]. Therefore, the count rate is interpreted as peaks in plotted XRD data. Matching XRD experimental peaks with known peaks recorded in diffraction databases (such as ICDD) allows for quick identification of specific materials (such as Si, Mo, In, and InP) based on their known crystal structure. Powder XRD database information can be used in conjunction with the the aforementioned equations to determine additional material parameters. For example, if a peak in the experimental data matches exactly with a known peak, the powder diffraction file (PDF) will list the Miller indices of that plane. With this information, everything is known to calculate the lattice constant of the crystal using Eqs. 2.1 and 2.2.

2.10.3 PHOTOLUMINESCENCE SPECTROSCOPY

PL spectroscopy is a nondestructive characterization technique designed to measure various optical properties of III-V semiconductor materials. When growing photovoltaic materials such as InP, InAs, InGaP, PL can be used to measure the material's impurity levels, defects, recombination mechanisms, surface structures, excited states, and bandgap. For the purposes of this thesis, PL was used to investigate the latter parameter while the former optical properties are beyond the scope of this research. Using a Horiba single point PL setup (532 nm, 0.75A, Si/Ge detector), the PL spectrum of polycrysatlline InP was measured to determine the material's bandgap. Additionally, bandgap and FWHM values were compared to that of single crystal InP to verify the optical quality of the material.

In general, PL spectroscopy works by first directing monochromatic light (532 nm in this case) on a material whose energy is greater (2.33 eV) than the bandgap of the material that is being measured. The light is then absorbed by the material initiating photo-excitation. In this phenomenon, a photon is absorbed by the material thereby transferring its energy to an electron in the atom's valance shell. This electron becomes excited and advances from the valance band to a higher energy level. If the energy absorbed by the electron is exactly the material's bandgap

(energy difference between valance and conduction bands), the electron will excite to exactly the conduction band edge. If the energy is larger than the bandgap, the electron will excite above the conduction band edge before relaxing back down to the conduction band edge via non-radiative process by dissipating excess energy to the lattice in the form of heat. Therefore, all excited electrons eventually relax to the conduction band edge and then back down to the valance band via radiative transmission resulting in photon emission with energy equal to the material's bandgap. The emission spectrum is then detected and sent to electronic equipment in the form of electrical pulses that are interpreted as a count rate which is proportional to the intensity of the emission spectrum. From this data, the material's bandgap can be determined by Gaussian distribution curve fitting methods to extrapolate the mean energy (or wavelength) of the spectrum [19].

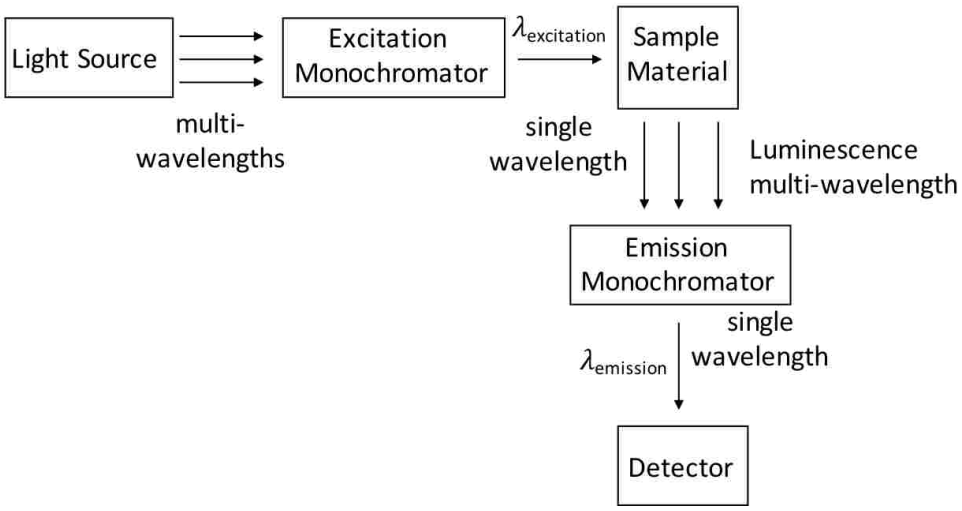

FIG. 2.10: Basic PL setup.

CHAPTER 3

RESULTS AND DISCUSSION

In this work, the TF-VLS method has been used to successfully achieve polycrystalline thin-film InP, InAs, and possible InGaP on Mo surfaces (Mo foil and/or sputtered Mo). This section will provide a comprehensive discussion and analysis of data resulting from SEM, EDX, XRD, and PL characterization.

3.1 TF-VLS GROWN InP ON Mo FOIL

Sample preparation and phosphorization of TF-VLS grown InP on Mo foil took place as described by section 2.6 and Fig. 2.7. The deposition parameters for the initial indium layer are as follows: 400 nm of In deposited at a rate of 2.1 nm/min at room temperature on electropolished Mo foil (25 µm) via RF sputtering with 30 W power and chamber pressure of 3 mT. The phosphorization of In took place in a laminar flow quartz tube style MOCVD reactor using a graphite sample susceptor for a duration of 20 minutes with a chamber temperature of 750°C and a partial P pressure of 6.23 mbars.

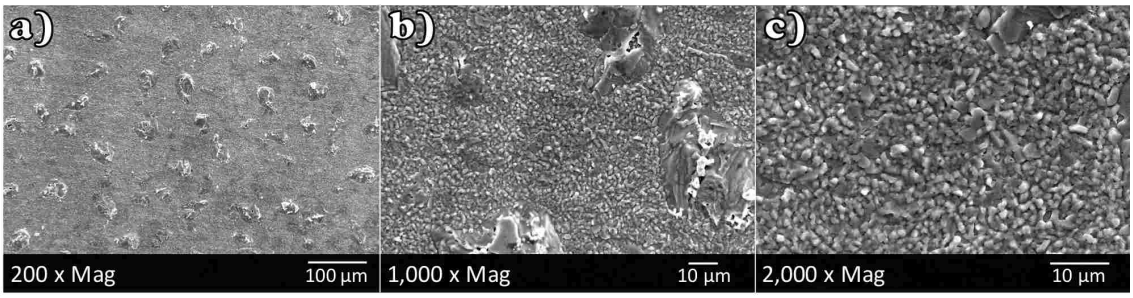

FIG. 3.1: SEM images of TF-VLS grown polycrystalline InP material on Mo foil taken at the same spatial location at magnifications of: a) 200X, b) 1,000X, c) and 2,000X.

Fig. 3.1 shows SEM images of TF-VLS grown InP on Mo foil. Fig. 3.1a shows 200x magnification of uniform surface coverage of indium phosphide islands with a density of approximately 200 islands per square millimeter. A closer look (Fig.

3.1b,c) reveals that the islands are surrounded by very small indium phosphide grains. This is confirmed by EDX measurements shown by Fig. 3.2 with images captured at a magnification of 2,000x at an island location. The red and blue images (lower right and left, respectively) show a spatial correlation of indium and phosphorous which helps to confirm that both In and P uniformly make up both island and non-island sites. The yellow image (upper right) suggests that the InP island is thick enough to limit the Mo signal at the location of the island. Cross-section SEM images are not currently available but would provide better indication of island height. While Fig. 3.1 and 3.2 demonstrate uniform InP coverage, the islands and small grains may prove problematic when developing a high performance photovoltaic device due to increased recombination sites. This emphasizes the need for an SiO_2 capping layer to maintain planar surface geometry by preventing dewetting of liquid indium during phosphorization. Studying the effects of the capping layer will be the next step in the pathway towards high-quality polycrystalline InP.

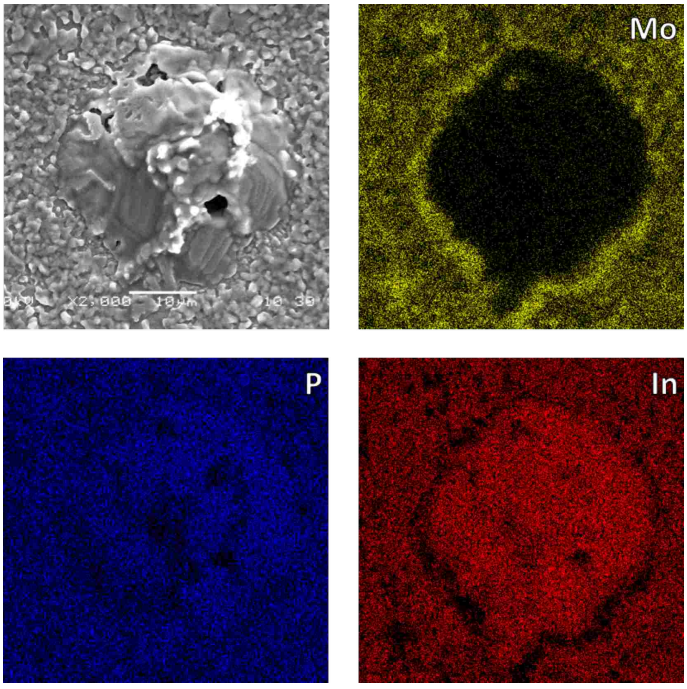

FIG. 3.2: EDX images of TF-VLS grown polycrystalline InP material on Mo foil taken at an island location corresponding to Mo (upper right), P (lower left), and In (lower right) material coverage.

Fig. 3.3a shows the powder XRD spectrum of the InP/Mo(foil) stack. XRD results are consistent with polycrystalline InP with peaks corresponding to multiple crystal planes. Most notable is the lack of pure unbound In peaks which would have occurred at 33, 36, and 40 degrees indicating full consumption of In by the formation of InP. Fig. 3.3b shows the normalized photoluminescence emission spectra of the experimental film compared to single crystalline InP substrate. Both the TF-VLS grown sample and the InP substrate emitted in close agreement to the InP bandgap of 1.34 eV. Although the intensity from the TF-VLS InP was much weaker than the substrate emission, it is encouraging that the full width-half-maximum (FWHM) for both measurements were nearly identical (50 and 57 meV, respectively) indicating similar optical quality material.

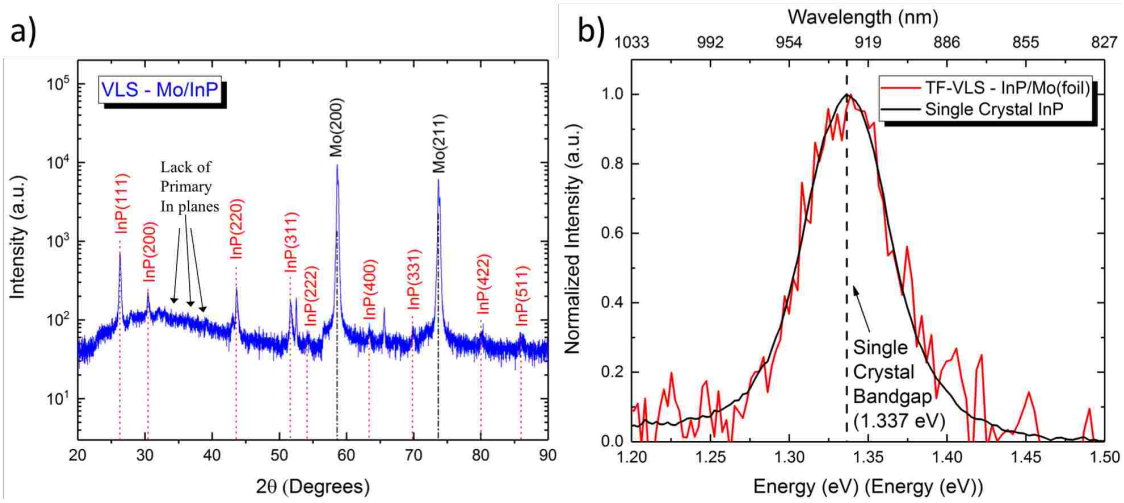

FIG. 3.3: TF-VLS grown polycrystalline InP material on Mo foil a) powder XRD, b) normalized PL with TF-VLS InP compared to single crystal InP substrate with bandgaps of 1.3374 and 1.3365 eV and FWHM values of 50.6 and 57.2 meV, respectively.

3.2 TF-VLS GROWN InP ON Mo/Si

Preparation and phosphorization of TF-VLS grown InP on Mo(700nm)/Si(wafer) took place as described by section 2.7 and Fig. 2.8. The deposition parameters for the sputtered Mo layer are as follows: 700 nm of Mo deposited via RF sputtering with 300 W power and chamber pressure of 3 mT at a rate of 6 nm/min at room temperature on an intrinsic ⟨100⟩ orientation Si wafer. Following this, 400 nm of In

was deposited via RF sputtering at a rate of 3 nm/min at room temperature with 30 W power and chamber pressure of 3 mT. Phosphorization of the In occurred for a duration of 25 minutes with a chamber temperature of 800°C and a partial pressure of 0.44 mbars.

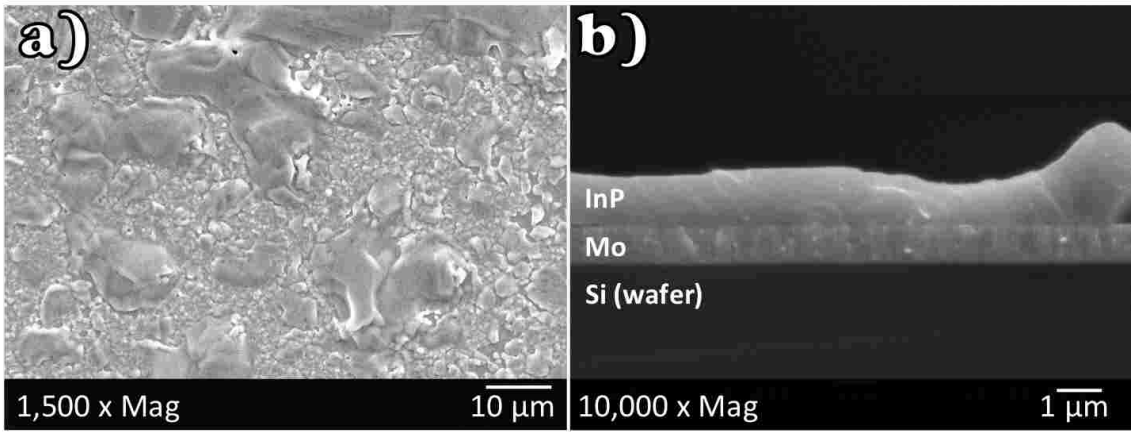

FIG. 3.4: a) 1,500x planar and b) 10,000x cross-section SEM images of TF-VLS grown polycrystalline InP material on Mo(700nm)/Si(wafer).

Fig. 3.4 shows planar and cross-section SEM images of TF-VLS grown InP on sputtered Mo. The planar image (Fig. 3.4a) shows surface morphology similar to the InP/Mo(foil) sample (Fig. 3.1) in that they both demonstrate rough island covered surfaces. However, this sample does appear to have somewhat smoother and more continuous islands than the foil sample. Cross-sectional imaging (Fig. 3.4b) shows a mostly uniform InP layer on Mo. However, this image was captured at a non-island location where the InP fully covered the Mo surface. The image is encouraging because it shows that the crystal growth can occur in a planar format without defects such as pinholes or voids throughout the InP layer.

Fig. 3.5a shows the powder XRD spectrum of the InP/Mo/Si stack which is consistent with polycrystalline InP with peaks corresponding to multiple crystal planes. As with the previous sample, these results demonstrate the lack of pure unbound In peaks which would have occurred at 33, 36, and 40 degrees indicating full consumption of In by the formation of InP. Fig. 3.5b shows the normalized photoluminescence emission spectra of the InP/Mo/Si stack compared to the single crystalline InP substrate. Both the TF-VLS grown sample and the InP substrate emitted in close agreement to the InP bandgap of 1.34 eV and share similar full-width-half-max

values indicating the optical properties of the TF-VLS grown sample are similar to that of single crystal InP.

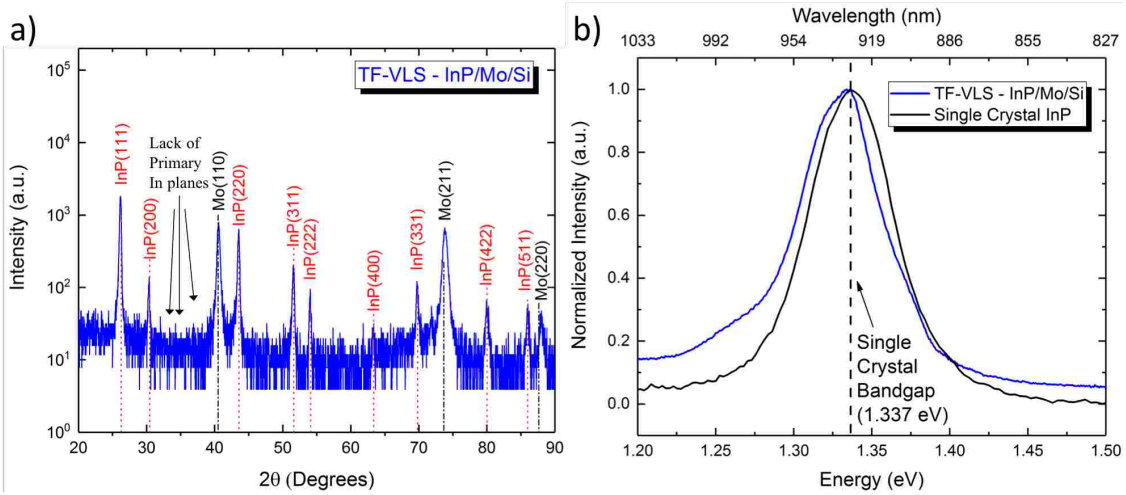

FIG. 3.5: TF-VLS grown polycrystalline InP material on Mo/Si a) powder XRD, b) normalized PL of TF-VLS InP compared to single crystal InP substrate with bandgaps of 1.3485 and 1.3365 eV and FWHM values of 52.3 and 57.2 meV, respectively.

3.3 TF-VLS GROWN InAs ON Mo FOIL

Preparation and phosphorization of TF-VLS grown InAs Mo foil took place as described by section 2.8 and Fig. 2.7. The deposition parameters for the initial indium layer are as follows: 400 nm of In was deposited via RF sputtering at a rate of 3 nm/min at room temperature with 30 W power and chamber pressure of 3 mT. The arsinization of In took place for a duration of 20 minutes with a chamber temperature of 750°C and a partial (phosphorous) pressure of 6.23 mbars.

Fig. 3.6 shows the powder XRD spectrum of the InAs on Mo foil. These results show clear InAs peaks but with several unidentified peaks. The lattice constants were calculated to be unusually high (6.3-7.3 Å), possibly indicating multiple InAs phases and/or antimony contamination.

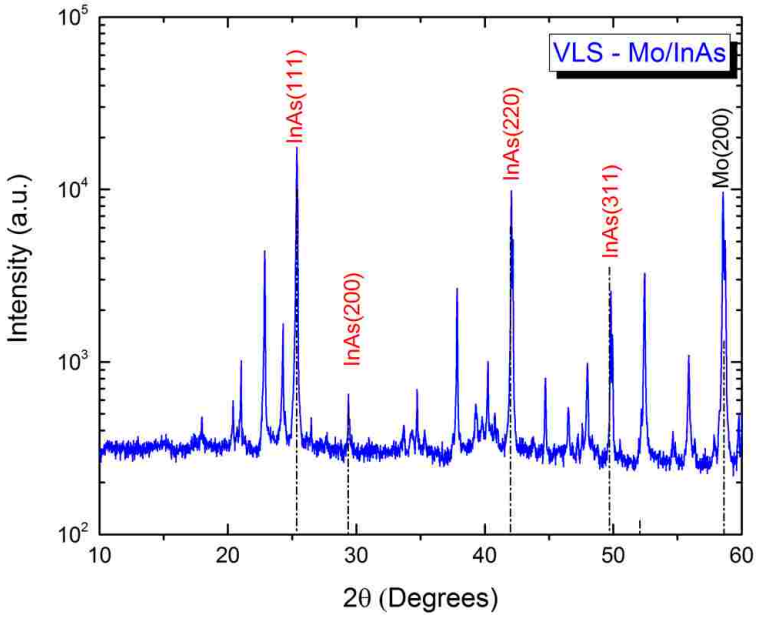

FIG. 3.6: Powder XRD of TF-VLS grown polycrystalline InAs material grown on Mo foil.

3.4 TF-VLS GROWN InGaP ON Mo FOIL

Preparation and phosphorization of TF-VLS grown InGaP on Mo foil took place as described by Section 2.9. A 1:1 ratio of In and Ga was deposited via co-evaporation at a rate of 1 Å/s and chamber pressure of 1 µTorr, resulting in a 400 nm layer of $In_{0.5}$ $Ga_{0.5}$ alloy. The phosphorization of InGa occurred for a duration of 20 minutes with a chamber temperature of 750°C and a partial P pressure of 6.23 mbars. Fig. 3.7 shows SEM images of preliminary TF-VLS InGaP growth efforts. At 1,500x magnification, Fig. 3.7a demonstrates rough surface morphology while Fig. 3.7b at 15,000x magnification reveals small, light colored phases on top of larger, darker phases. Photoluminesce of the InGaP trial (Fig. 3.8) illustrate five distinguishable peaks corresponding to bandgaps ranging from 1.28-1.65 eV, possibly indicating different phases of InGaP or materials other than the intended InGaP. For example, the PL spectra of the single crystalline InP substrate is shown to fit the main peak in the InGaP spectra (emitting at a bandgap of 1.337 eV). This could suggest possible disassociation of InGa which would allow In to phosphorize into InP.

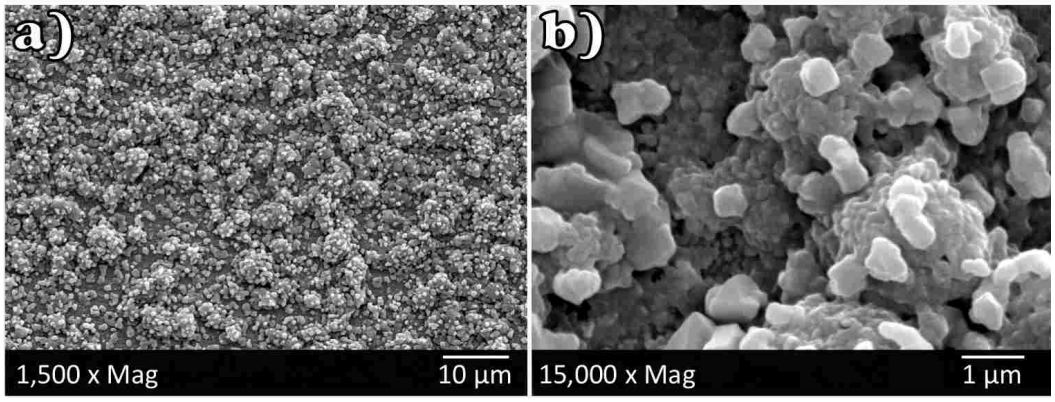

FIG. 3.7: SEM images of possible InGaP material grown on Mo foil using TF-VLS process a) 1,500X, b) 15,000X.

The two peaks to the left of the possible InP peak emit at lower bandgaps (1.27-1.30 eV). This bandgap range is consistent with arsenic species such as GaAs, InAs, or InGaAsP which could indicate arsenic contamination of the MOCVDs quartz chamber lining. This bandgap range is also consistent with other phases of InP. Therefore, phosphorization of InGa may have occurred, however further material characterizations are necessary for conclusiveness.

3.5 PHOSPHORIZATION STUDIES

The first section in this chapter (3.1) discussed a very early trial of the TF-VLS growth of InP on Mo foil. The second section featured a sample that was part of a variety of studies aimed to investigate InP optimization growth parameters. Table 3.1 lists all involved samples, substrates, and their initial In deposition and phosphorization parameters while Fig. 3.9 shows corresponding SEM images. The process steps for all samples were as described in Section 2.6 and 2.7 and illustrated in Figs. 2.7 and 2.8 which began with the growth of 400 nm of In on either Mo foil or Mo sputtered on an intrinsic $\langle 100 \rangle$ orientation Si wafer. For the latter, 700 nm of Mo was deposited via RF sputtering with 300 W power and chamber pressure of 3 mTorr at a rate of 6 nm/min at room temperature. The following sections will discuss in detail three primary growth parameters that affect InP growth: growth temperature of the initial In deposition, phosphorization temperature, and the partial pressure

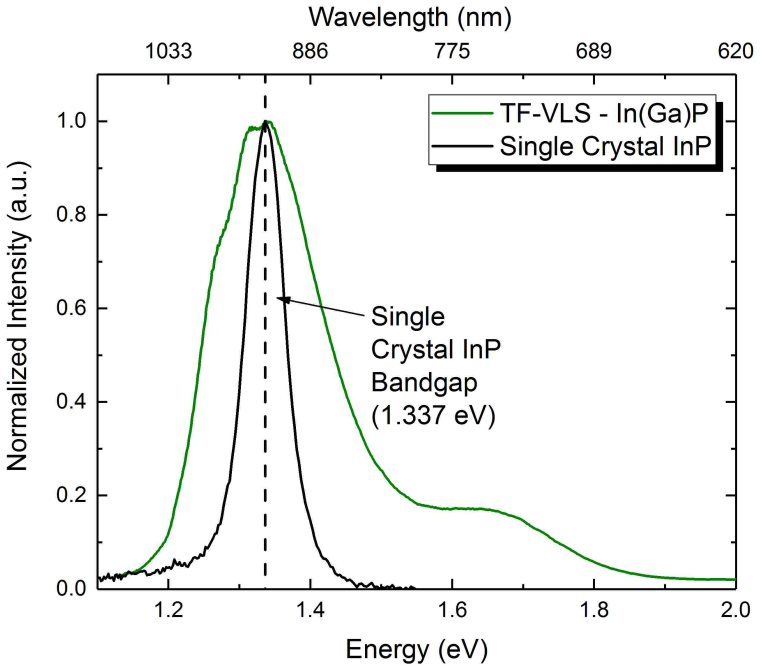

FIG. 3.8: Normalized photoluminesce of TF-VLS grown polycrystalline InGaP material on Mo foil compared to single crystal InP substrate.

of P gas flow. Techniques such as SEM, XRD, and PL are used to characterize the resulting InP film.

3.5.1 INITIAL In DEPOSITION TEMPERATURE

For this study, the temperature of the Mo foil substrate was varied during the deposition of the indium layer in order to investigate this effect on the resulting InP film. The samples involved in this study can be found listed in Table 3.2. Both samples share the same growth parameters (substrate, deposition method, deposition rate, and phosphorization pressure, temperature, and time) with the exception of the growth temperature of the initial indium layer. On Mo foil substrates, one sample was grown at room temperature (22°C) while the other was grown with the substrate heated to 200°C.

The XRD spectrum of the resulting InP layer shown in Fig. 3.10a shows that both samples have pure unbound indium peaks occurring at 33, 36, and 40 degrees. Since both samples demonstrate this effect, this is likely independent of indium growth

TABLE 3.1: TF-VLS InP growth parameters. For all Si/Mo samples, 700 nm of Mo was deposited via RF sputtering with 300 W power and chamber pressure of 3 mTorr at a rate of 6 nm/min at room temperature on an intrinsic ⟨100⟩ orientation Si wafer. For all samples, the deposition thickness of In remained constant at 400nm.

		Indium Deposition (400 nm)			**Phosphorization**		
Sample Number	Substrate type	Method	Temp [°C]	Rate [nm/min]	PP [mbar]	Temp [°C]	Time [min]
16R202	Si/Mo	RF Sputter	22	3	4.31	650	25
16R204	Si/Mo	RF Sputter	22	3	0.44	650	25
16R206	Si/Mo	RF Sputter	22	3	0.09	650	25
16R207	Si/Mo	RF Sputter	22	3	0.44	700	25
16R203	Si/Mo	RF Sputter	22	3	8.25	650	25
16R205	Si/Mo	RF Sputter	22	3	4.31	600	25
16B005	Mo foil	Thermal	200	15	4.67	750	5
16B004	Mo foil	Thermal	22	15	4.67	750	5

TABLE 3.2: Initial In deposition temperature study.

		Indium Deposition (400 nm)			**Phosphorization**		
Sample Number	Substrate type	Method	Temp [°C]	Rate [nm/min]	PP [mbar]	Temp [°C]	Time [min]
16B004	Mo foil	Thermal	**22**	15	4.67	750	5
16B005	Mo foil	Thermal	**200**	15	4.67	750	5

temperature. These sample were only phosphorized for a total of 5 minutes and therefore it would be reasonable to believe that longer exposure times would complete the In consumption process considering previously shown samples that demonstrated the absence of In peaks were phosphorized at 20 minutes or longer (Fig. 3.3). It is also reasonable to assume that the flexibility of the Mo substrate did not allow for uniform heat transfer, thereby preventing uniform In phosphorization. The PL spectrum shown in 3.10b shows both samples emit in close agreement with the InP bandgap of 1.34 eV, share similar FWHM values, and emit at nearly the same intensity indicating that of similar optical quality materials. The sample with In growth temperature of 22°C does emit a secondary peak to the left of the primary peak indicating the presence of impurities or traps. The exact cause of the peak is unclear as it appears in

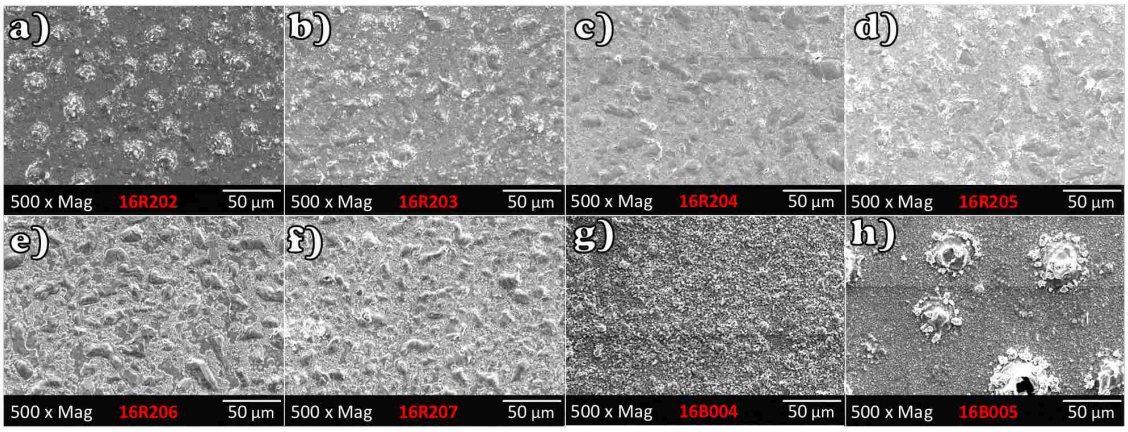

FIG. 3.9: TF-VLS grown InP corresponding to samples listed in Table 3.1.

only 3 of the 8 samples shown in Table 3.1 of which no correlation could be presently identified. This trap feature is discussed in greater length in Section 3.5.4.

Thus far, XRD and PL have not indicated that the the crystallinity or optical quality of the material is affected by substrate heating during In deposition, however, SEM images (Fig. 3.11) captured at only 50x magnification show a clear difference in surface morphology. The sample with In grown at 200°C demonstrates rough island covered surface while the sample with indium grown at room temperature appears much planar in comparison. The island features are likely due to the In dewetting from the Mo foil surface due to an increased temperature during the deposition of the initial In layer. The effects of In deposition on heated Mo foil will be revisited in Section 3.6.3.

To conclude this study, varying initial indium deposition temperatures does not seem to have a pronounced effect on crystallinity or optical quality of the material. However, SEM images show a clear difference in surface morphology. A solar cell grown on the sample with In deposited on heated Mo foil may prove inferior to one grown on room temperature deposited In due to the island features that would translate into structural defects when subsequent layers are grown.

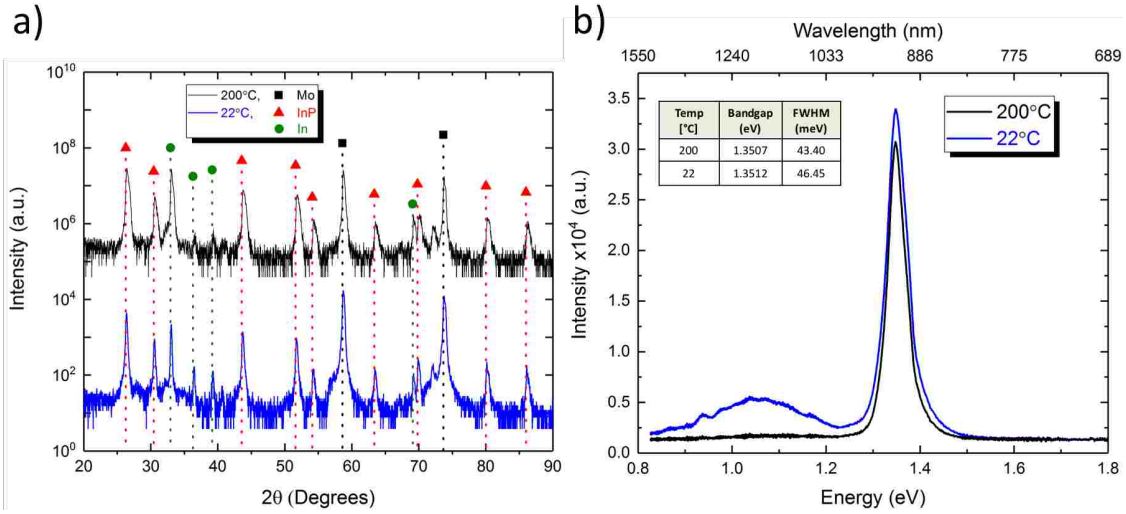

FIG. 3.10: TF-VLS grown InP on Mo foil with varying initial indium deposition temperatures: a) XRD, b) PL.

3.5.2 PHOSPHORIZATION TEMPERATURE

For this study, the temperature at which the In is phosphorized is investigated at two different partial pressures. The growth parameters are shown in Table 3.3 where the InP growth occurred on Si/Mo substrates in the manner described in Section 2.7. First, phosphorization occurred at a partial pressure of 4.31 mbars at temperatures

TABLE 3.3: Phosphorization temperature study.

		Indium Deposition (400 nm)			**Phosphorization**		
Sample Number	Substrate type	Method	Temp [°C]	Rate [nm/min]	PP [mbar]	Temp [°C]	Time [min]
16R207	Si/Mo	RF Sputter	22	3	0.44	**700**	25
16R204	Si/Mo	RF Sputter	22	3	0.44	**650**	25
16R202	Si/Mo	RF Sputter	22	3	4.31	**650**	25
16R205	Si/Mo	RF Sputter	22	3	4.31	**600**	25

of 750 and 800°C, then at the lower partial pressure of 0.44 mbars at temperatures of 800 and 850°C for 25 minutes. All In growth occurred at room temperature via RF sputtering at a deposition rate of 3 nm/min.

Fig. 3.12 shows XRD and PL spectrums of the resulting InP film grown at a

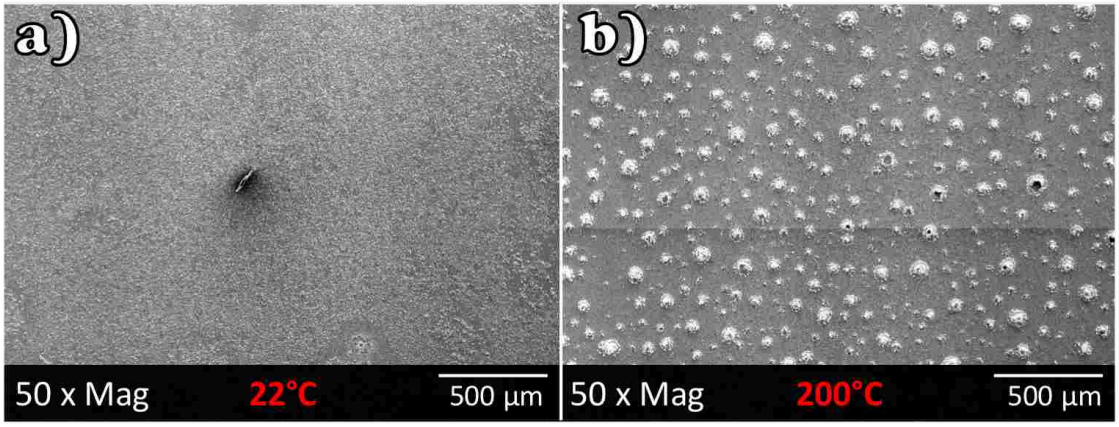

FIG. 3.11: SEM images of TF-VLS grown InP on Mo foil with varying initial indium deposition temperatures.

partial pressure of 4.31 mbars. The XRD results indicate the absence of In peaks indicating full consumption of In by InP formation. This is not surprising given a phosphorization time longer than 20 minutes and a rigid substrate providing for more uniform heat transfer compared to Mo foil. As with previous samples, the PL spectrum emits close to the InP bandgap of 1.34 eV and both samples share similar FWHM values. However, the sample grown at the higher temperature of 800°C emits at a greater intensity indicating higher optical quality material due to a more efficient radiative recombination process. The lower temperature sample emits an impurity/trap peak to the left of the main peak as seen before. The end of this section will provide a comprehensive discussion of all samples that demonstrate this feature.

Fig. 3.13 shows XRD and PL spectrums of InP film grown at a partial pressure of 0.44 mbars. As with the previous phosphorization temperature study, the XRD spectrum shows the lack of unbound In peaks indicating full In consumption by the phosphorization process. PL characterization shows a shift in bandgap emission with a difference of 23 meV between samples. The higher temperature sample emits further from the InP bandgap of 1.34 eV. PL mapping of this sample may prove spatial dependence on bandgap emission. The red-shift in both samples could be related to the varying shapes and sizes of the crystallites as shown by SEM images in Fig. 3.9. Structural disorder has a profound influence on the optical properties of

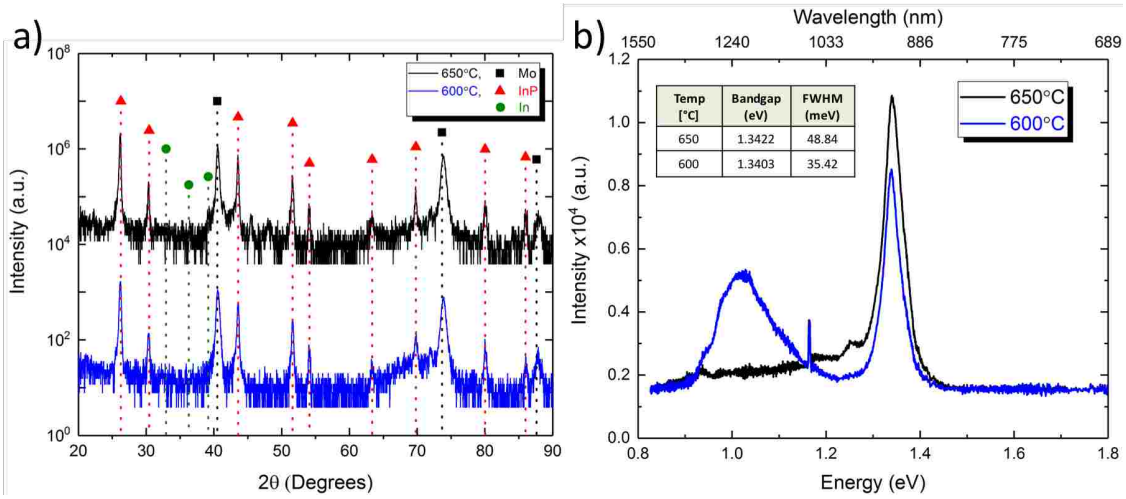

FIG. 3.12: TF-VLS grown InP on Mo/Si with varying phosphorization temperatures at a partial pressure of 4.31 mbars: a) XRD, b) PL.

the material [20]. If PL was performed on a raised feature (or island) on one sample and a more planar feature on the other, it is possible for the samples to emit at slightly varying bandgaps. As with the previous phosphorization temperature study, the sample grown at the higher temperature (this time 850°C) emits at a greater intensity indicating higher optical quality material.

To conclude this study, varying phosphorization temperatures does not seem to have a pronounced effect on crystallinity but does seem to have an effect on the optical quality of the material. For both studies, at two different partial pressures, the PL intensity for the InP grown at the higher temperature was greater than InP grown at the lower temperature, thereby indicating higher optical material in both samples grown at the higher temperatures.

3.5.3 PARTIAL PRESSURE

In this final phosphorization study, the partial pressure of P gas flow through the chamber is varied to investigate its effect on the resulting InP material. The growth parameters of the samples in this study are shown in Table 3.4 where all In was grown at 3 nm/min via RF sputtering on an Si/Mo substrate prior to phosphorization which took place at 800°C for 25 minutes at four different partial pressures ranging from

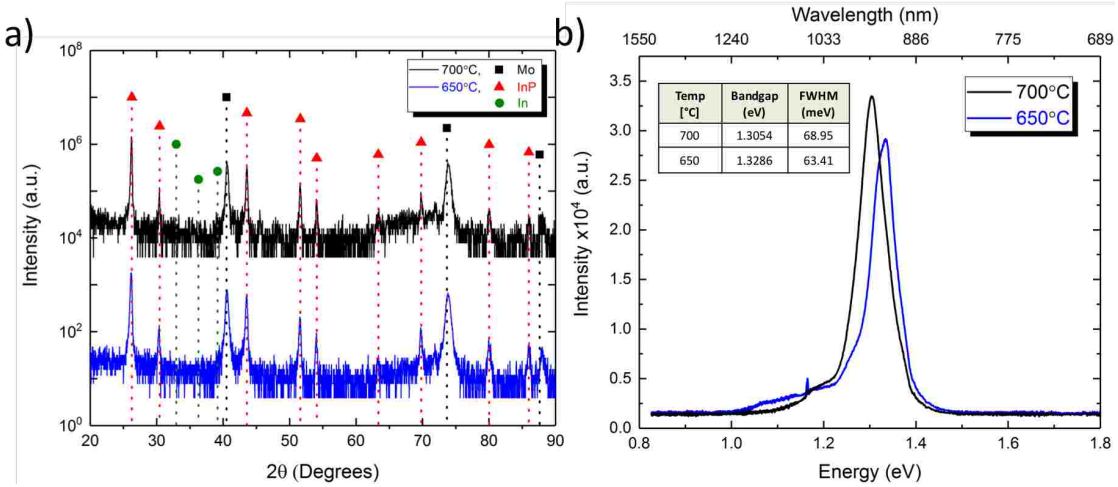

FIG. 3.13: TF-VLS grown InP on Mo/Si with varying phosphorization temperatures at a partial pressure of 0.44 mbars: a) XRD, b) PL.

TABLE 3.4: Partial pressure study.

		Indium Deposition (400 nm)			Phosphorization		
Sample Number	Substrate type	Method	Temp [°C]	Rate [nm/min]	PP [mbar]	Temp [°C]	Time [min]
16R206	Si/Mo	RF Sputter	22	3	**0.09**	650	25
16R204	Si/Mo	RF Sputter	22	3	**0.44**	650	25
16R202	Si/Mo	RF Sputter	22	3	**4.31**	650	25
16R203	Si/Mo	RF Sputter	22	3	**8.25**	650	25

0.09 to 8.25 mbar.

Fig. 3.14 shows XRD and PL spectrums of the resulting InP films. The powder XRD results are again consistent with polycrystalline InP and lack pure unbound In peaks for all samples. The intensities and widths of the peaks do not vary between samples indicating no crystallinity dependence on partial pressure. All samples in the PL spectrum emit close to the InP bandgap of 1.34 eV, however, the samples as the higher partial pressures emit closer to 1.34 than the two at the lower pressures. As with the previous study (Fig. 3.13) the red-shift this study could be related to the varying shapes and sizes of the crystallites as shown by SEM images in Fig. 3.9.

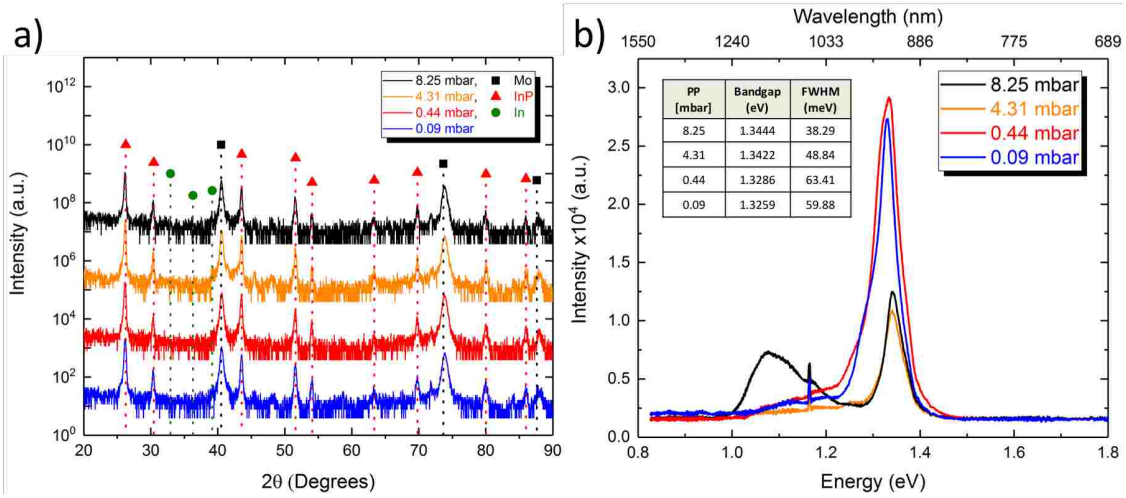

FIG. 3.14: TF-VLS grown InP on Mo/Si with varying partial pressures: a) XRD, b) PL.

Structural disorder has a profound influence on the optical properties of the material [20]. Also noticeable are the intensities of the two lower pressure samples emit much higher than the higher pressure samples indicating higher radiative recombination efficiency. All indications point to partial pressure dependence on the optical quality of the material.

3.5.4 PL DISCUSSION

Table 3.5 lists the bandgaps, FWHM, variation from the accepted InP bandgap value of 1.444eV, whether an impurity/trap peak was emitted, and if XRD indicated pure unbound In for the 8 samples previously discussed. FWHM values of the 8 samples had a mean of 50.6 meV, standard deviation of 12.2 meV, with a range of 34 meV. All 8 samples emitted close to the InP bandgap of 1.34 eV with a mean of 1.336 eV, standard deviation of 15.4 meV, and range of 46 meV with a noticeable blue shift for 2 samples and a red shift for 5 samples. The shifts can be attributed to the varying sizes of the crystallites that make up the InP film which can cause carrier confinement. Due to this effect, larger values of the bandgap occur in the crystallites having the smallest sizes and vice versa [20]. Therefore, there is a spatial dependence on the bandgap emission depending on whether the location of the of

TABLE 3.5: TF-VLS InP PL and XRD Results.

	Photoluminesce				XRD
Sample Number	E_g [eV]	E_g-1.344 [meV]	FWHM [meV]	Impurity Peak [eV]	Unbound In Peaks [yes/no]
16R202	1.3422	-2	49	N/A	no
16R204	1.3286	-15	63	N/A	no
16R206	1.3259	-18	60	N/A	no
16R207	1.3054	-39	70	N/A	no
16R203	1.3444	0	39	1.1037	no
16R205	1.3403	-4	35	1.0293	no
16B005	1.3507	+7	43	N/A	yes
16B004	1.3512	+7	47	1.0590	yes

the PL measurement was at a small or large crystal site.

The impurity/trap peak occurred in 3 of the 8 samples and show no real correlation between any one condition. As indicated by Table 3.1, one of the samples was grown on Mo foil and the other two on Si/Mo. The In growth of two samples were via RF sputtering and the other via thermal evaporation with deposition rates of 3 and 15 nm/min, respectively. All samples that emitted the peak were phosphorized at different partial pressures. Two samples were phosphorized for 25 minutes with the other for 5 minutes. Phosphorization temperatures varied for two of the three samples and they were all part of separate phosphorization studies. Additionally, the InP of one of the samples was grown at NASA Glenn Research Center while the other two were grown at RIT. There is no clear indication of the impurity/trap peak's origin. Speculation would suggest the introduction of contaminants during handling or of the PL equipment.

3.6 INITIAL In LAYER OPTIMIZATION

One of the very first TF-VLS experiments performed during this research was to attempt polycrystalline InP growth by phosphorizing a SiO_2(50nm)/In(400nm)/Mo(foil) stack using the process described by Kapadia at el. outlined in Section 2.6 and illustrated in Fig. 2.6. As a result, XRD and PL indicated that InP failed to form and it was determined that the SiO_2 layer was being broken up and removed during the process. This was likely due to the rough initial

In surface. With the island and small grain surface morphology previously shown (Fig. 3.1), during phosphorization those islands and grains would grow upward and outward as In and P atoms bind. With an SiO_2 layer on top of that type of surface, the SiO_2 also grows up and outward until the layer broke up due to stress from the mulit-directional material growth beneath it. With a more planar surface, the SiO_2 layer will grow upward (single directional) and not multi-directional, thereby serving its function by keeping the growing atoms beneath it from dewetting on the Mo foil surface. The growth of a planar InP surface provides for longer grain boundaries which limit electron/hole recombination locations. The next series of studies aims to resolve the rough In surface that makes the use of SiO_2 problematic. The studies begin with a RF sputtering deposition pressure study. The pressure that resulted in the most planar In surface was then held constant during the power study. Again, the power that resulted in the most planar surface was then held constant for the temperature study. Finally, electron beam deposition is investigated while varying the In deposition rate. Then the two deposition methods are directly compared.

3.6.1 PRESSURE STUDY

For this study, 400 nm of In was deposited on Mo foil at room temperature via RF sputtering at a power of 30 W and pressures ranging from 1.1 to 15 mTorr. Deposition parameters are listed in Table 3.6.

TABLE 3.6: In deposition pressure study.

Time [min]	Rate [Å/s]	Pressure [mTorr]	Power [W]	Temperature [°C]
50	1.3	**1.1**	30	22
66	1.0	**3.0**	30	22
133	0.5	**15**	30	22

Fig 3.15 shows SEM images at 2,500x and 20,000x magnification of the resulting In surfaces. The images demonstrate progressively vacant In surface coverage as the deposition pressure increases. Increased chamber pressure makes it more difficult for In atoms to find the substrate. As the pressure increases, the In has an increased number of other atoms (in this case Ar) to collide with thereby reducing the probability that an In atom will reach the substrate. Therefore, the pressure that resulted

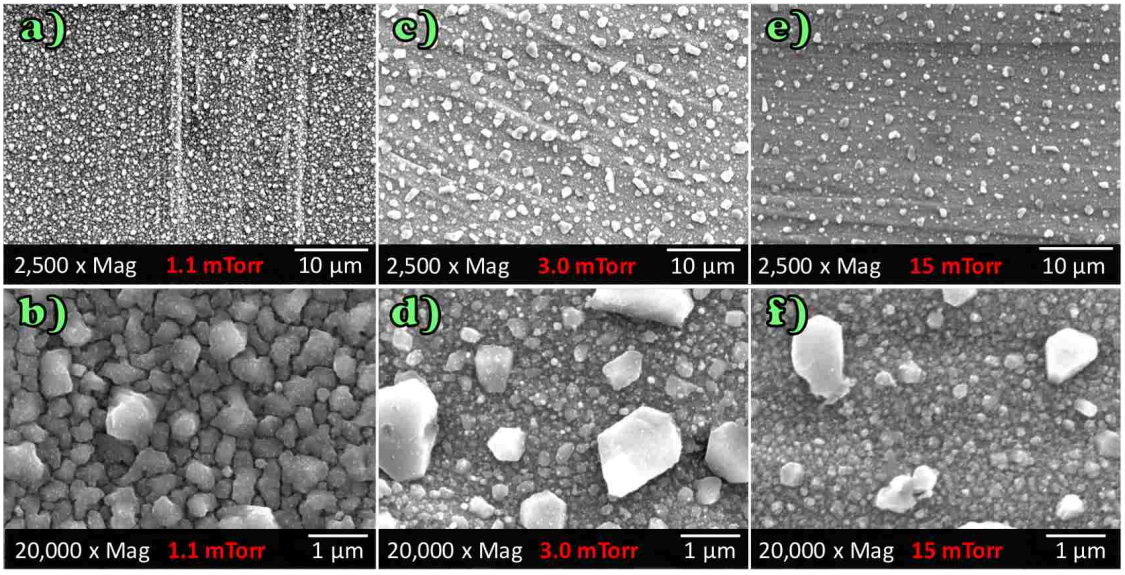

FIG. 3.15: SEM images of 400 nm of In deposited at room temperature via RF sputtering at a power of 30 W and pressures ranging from 1.1 to 15 mTorr.

in the most complete In surface coverage is 1.1 mTorr (Fig. 3.15a,b) and was held constant for the next study, power.

3.6.2 POWER STUDY

For this study, 400 nm of In was deposited on Mo foil at room temperature via RF sputtering at a pressure of 1.1 mTorr with RF power ranging from 13 to 50 W. Deposition parameters are listed in Table 3.7.

TABLE 3.7: In deposition power study.

Time [min]	Rate [Å/s]	Pressure [mTorr]	Power [W]	Temperature [°C]
133	0.5	1.1	**13**	22
50	1.3	1.1	**30**	22
27	2.3	1.1	**50**	22

Fig. 3.16 shows SEM images of the resulting In surface morphology at 2,500 and 20,000x magnification. Even at this high magnification, it is very difficult to

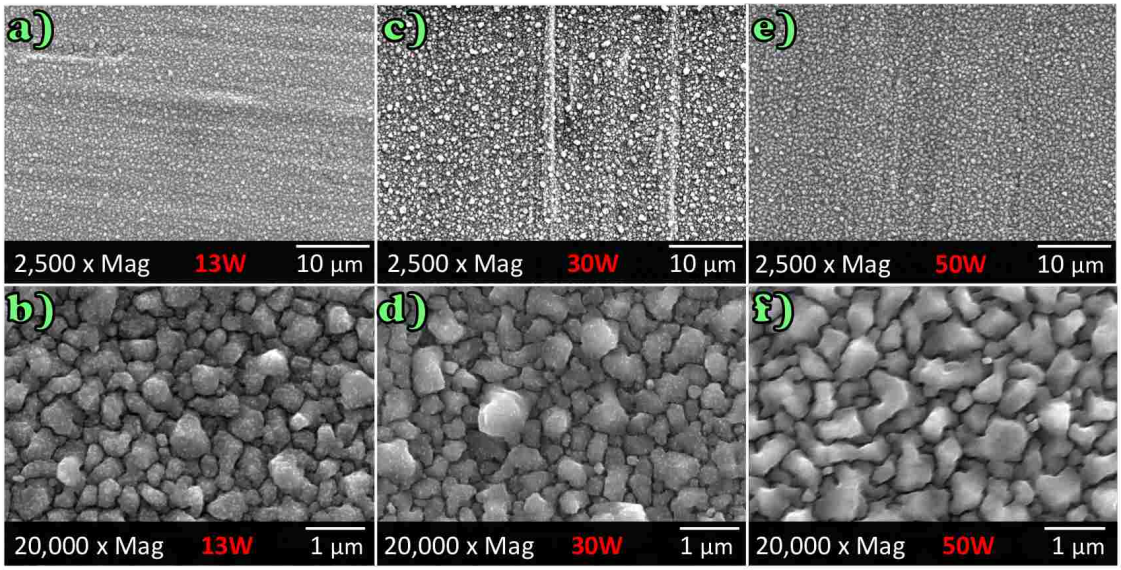

FIG. 3.16: SEM images of 400 nm of In deposited on Mo foil at room temperature via RF sputtering at a pressure of 1.1 mTorr with RF power ranging from 13 to 50 W

determine which sample has a more favorable surface morphology as they all look similar in coverage and have similarly shaped grains. It is believed that, for indium, the higher the deposition rate the smoother the surface becomes. For this reason, the highest power (50 W) was chosen to remain constant for the following temperature study. The highest allowable power rated for the In sputtering target is 106 W which leave some room for future In studies at greater RF power.

3.6.3 TEMPERATURE STUDY

For this study, 400 nm of In was deposited on Mo foil a at pressure of 1.1 mTorr, a power of 50 W, and substrate temperatures ranging from 22 to 200°C. Deposition parameters are shown in Table 3.8.

Fig. 3.17 shows SEM images of the resulting In surface morphology at 2,500x and 10,000x magnification. The images show that as the substrate temperature increases from room temperature to 200°C, the In becomes more segregated. In Fig. 3.17c, the highest temperature, the Mo foil grains are clearly visible. This effect is due to the In increasingly dewetting as the surface energy between In and the Mo foil

TABLE 3.8: In deposition temperature study.

Time [min]	Rate [Å/s]	Pressure [mTorr]	Power [W]	Temperature [°C]
27	2.3	1.1	50	**22**
27	2.3	1.1	50	**100**
27	2.3	1.1	50	**200**

decreases, causing the liquid In to relax. It is believed that, for In, the lower the temperature the more planar the surface morphology becomes, which is consistent with the outcome of this study. A substrate cooling system would be required to deposit In at lower than room temperature which is more cumbersome than the technology used for substrate heating, making cooled In deposition a troublesome route to achieve quality In surface morphology. It seems this path can be more easily achieved through increased In deposition rates, which is the focus of the final study.

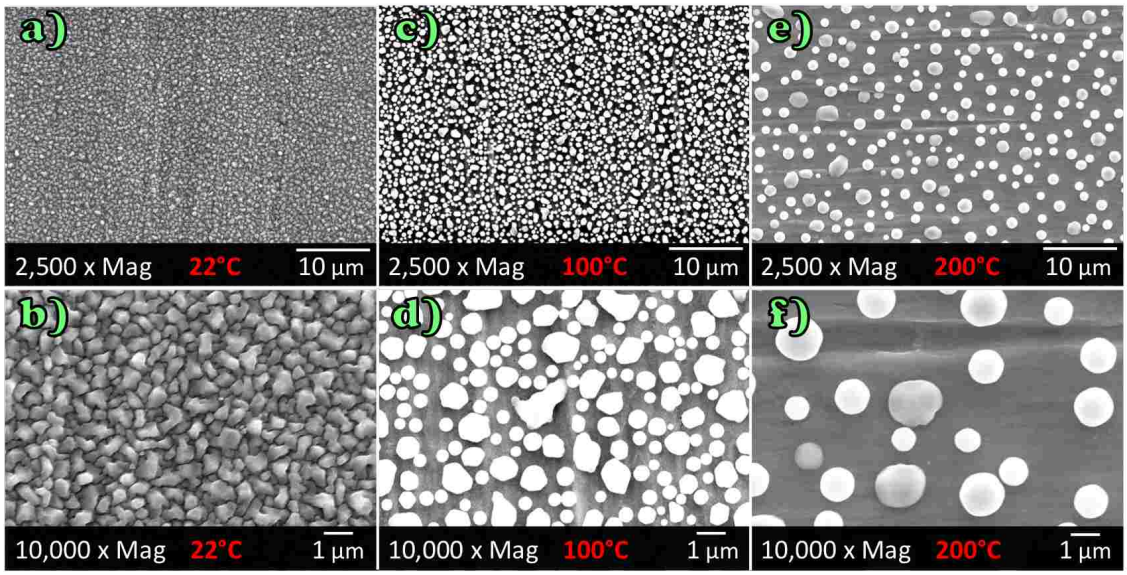

FIG. 3.17: SEM images of 400 nm of In deposited on Mo foil at a pressure of 1.1 mTorr, a power of 50 W, and substrate temperatures ranging from 22 to 200°C

3.6.4 EBEAM DEPOSITION RATE/THICKNESS STUDY

The primary objective of this study was to determine how smooth (or planar) the In surface could get after simultaneously increasing both the In deposition rate and layer thickness. For this study, between 0.4 and 2 µm of In was deposited on Mo foil at room temperature at deposition rates ranging from 2 to 100 Å/s. The deposition parameters are listed in Table 3.9.

TABLE 3.9: Electron beam In deposition study.

Time [min]	Rate [Å/s]	Thickness [µm]	Beam Voltage [kV]	Beam Current [mA]
37	**2**	**0.4**	8	7
4	**60**	**1.5**	8	19
3	**100**	**2.0**	8	23

Fig. 3.18 shows SEM images of the resulting In surface morphology at 2,500x and 10,000x magnification. The images show that as the deposition rate and layer

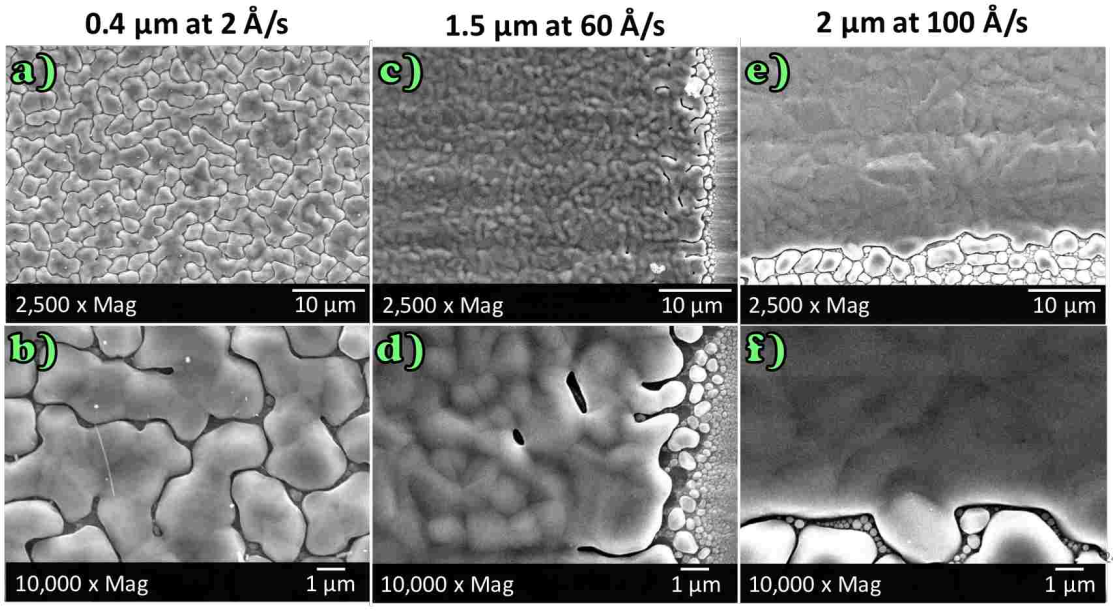

FIG. 3.18: SEM images of 0.4 to 2 µm of In deposited on Mo foil at room temperature with deposition rates ranging from 2 to 100 Å/s.

thickness are increased, features on the surface become less defined as the layer

appears smoother. At 2 Å/s and 0.4 µm, surface features are well defined. They begin to appear blurry at 60 Å/s and 1.5 µm and are almost invisible at 100 Å/s and 2 µm making it difficult to image without finding the edge of the In surface, thereby demonstrating an ideal surface for InP growth.

To better compare deposition methods, Fig. 3.19 shows the 2 Å/s and 0.4 µm image from above compared to 0.4 µm of In deposited via RF sputtering with similar deposition rates. Even at this low deposition rate, the grain sizes on the electron beam deposited surface are well defined and appear large whereas on the RF sputtering deposited surface the grain sizes are much smaller in comparison. Therefore, the surface demonstrated by Fig. 3.19a,b appears vastly superior to its RF sputtering counterpart, making electron beam deposition the preferred In deposition method for the growth of high quality polycrystalline InP (and other binaries and ternaries).

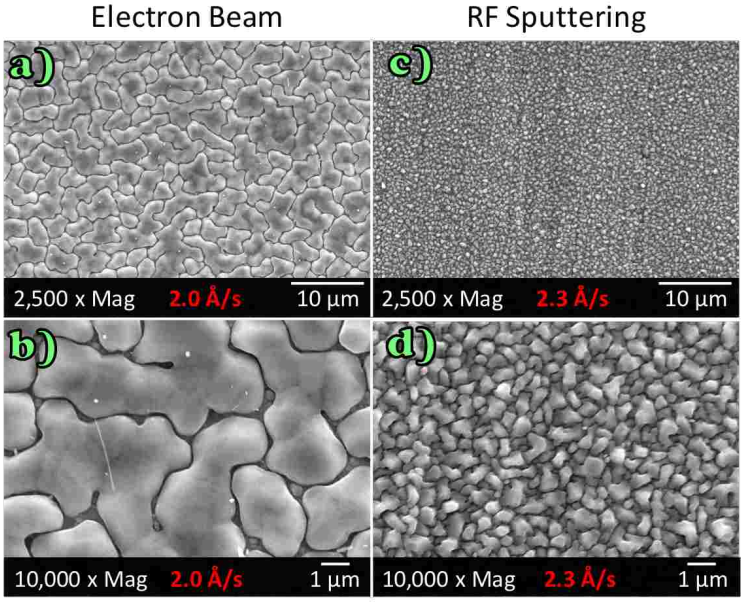

FIG. 3.19: 400 nm of In deposited at room temperature on Mo foil at similar deposition rates via: a,b) electron beam, c,d) RF sputtering deposition methods.

CHAPTER 4

CONCLUSION

This thesis demonstrates the successful TF-VLS growth of InP and InAs and the possible growth of InGaP on Mo foil and/or Mo sputtered on Si wafers. SEM images of InP/Mo(foil) and InP/Mo/Si show uniform surface coverage of indium phosphide islands surrounded by small indium phosphide grains thereby emphasizing the need for an SiO_2 capping layer to maintain planar surface geometry of liquid indium during phosphorization. Powder XRD spectra for the samples are consistent with polycrystalline InP with peaks corresponding to multiple crystal planes and lack pure unbound In peaks indicating full consumption of In by InP formation. Normalized photoluminescence shows TF-VLS and single crystal InP emit in close agreement to the InP bandgap of 1.34 eV and share comparable FWHM values indicating the two samples are of similar optical quality. InAs/Mo(foil) XRD results show clear InAs peaks but with a number of unidentified peaks suggesting possible antimony contamination. Photoluminesce of the InGaP/Mo(foil) trial illustrates five distinguishable peaks corresponding to bandgaps ranging from 1.28-1.65 eV, possibly indicating different phases of InGaP or materials other than the intended InGaP. Therefore, phosphorization of InGa may have occurred, however further material characterizations are necessary for conclusiveness.

This thesis also features a number of studies aimed at studying the effects of varying phosphorization parameters such as temperature and partial pressure. As a result, it was found that varying phosphorization temperatures does not seem to have a pronounced effect on crystallinity but does seem to have an effect on the optical quality of the material. For both studies, at two different partial pressures, the PL intensity for the InP grown at the higher temperature was greater than InP grown at the lower temperature, thereby indicating higher optical quality material in both samples grown at the higher temperatures. The partial pressure study shows PL intensities of samples phosphorized at lower pressures emit much higher than those phosphorized at higher pressures indicating higher radiative recombination efficiency and a clear partial pressure dependence on the optical quality of the material.

The final study featured in this work was aimed to optimize the In surface prior to phosphorization by varying RF sputtering deposition parameters such as pressure, power, and temperature in addition to a direct comparison of RF sputtering and electron beam deposition methods. Lower RF sputtering deposition pressures were shown to be ideal due to better In surface coverage. The power study was inconclusive due to the small variation in deposition rates (0.5-2.3 Å/s) given the larger variation in power (13-50 W). It is believed that In deposited at larger rates produces a smoother more continuous layer. The highest allowable power rated for the In sputtering target used is 106 W which leaves some room for future In studies at greater RF power. SEM images of In deposited at varying temperatures show that as the substrate temperature increases from room temperature to 200°C, the In becomes more segregated. Therefore, depositions at room temperature produces a more continuous (and favorable) In layer than at higher temperatures. The electron beam evaporation study simultaneously varied both the deposition rate and layer thickness resulting in progressively smoother/continuous In layer formation as both parameters are increased. Electron beam and RF sputtering comparisons, both at the low deposition rate of 2 Å/s, revealed large and well defined grain sizes on the electron beam deposited surface whereas the RF sputtering deposited surface demonstrates grains that are much smaller in comparison, thereby indicating the former method to be vastly superior to the latter.

BIBLIOGRAPHY

[1] U.S. Energy Information Administration. Total primary energy consumption 2014. [Online]. Available: https://www.eia.gov/beta/international

[2] J. Conti, "International energy outlook 2016," U.S. Department of Energy, Tech. Rep., 2016. [Online]. Available: https://www.eia.gov/outlooks/ieo/

[3] D. Bedford, *Climate Change Examining the Facts*, ser. Contemporary Debates, 2016.

[4] A. Luque and S. Hegedus, *Handbook of Photovoltaic Science and Engineering*. John Wiley & Sons, 2011.

[5] U.S. Energy Information Administration. Total carbon dioxide emissions from the consumption of energy 2014. [Online]. Available: https://www.eia.gov/beta/international

[6] K. Mertens, *Photovoltaics Fundamentals, Technology and Practice.*, ser. ebrary Academic Science and Technology Collection. Hoboken: Wiley, 2013.

[7] J. Nelson, *The Physics of Solar Cells*. London : Singapore ; River Edge, NJ: Imperial College Press ; Distributed by World Scientific, 2003.

[8] M. A. Green, K. Emery, K. Bcher, D. L. King, and S. Igari, "Solar cell efficiency tables (version 10)," *Progress in Photovoltaics: Research and Applications*, vol. 5, no. 4, pp. 265–268, 1997.

[9] M. A. Green, Y. Hishikawa, W. Warta, E. D. Dunlop, D. H. Levi, J. Hohl-Ebinger, and A. W. Ho-Baillie, "Solar cell efficiency tables (version 50)," *Progress in Photovoltaics: Research and Applications*, vol. 25, no. 7, pp. 668–676, 2017, pIP-17-089.

[10] R. Kapadia, Z. Yu, H. Wang, M. Zheng, C. Battaglia, M. Hettick, D. Kiriya, K. Takei, P. Lobaccaro, J. Beeman, J. Ager, R. Maboudian, D. Chrzan, and A. Javey, "A direct thin-film path towards low-cost large-area III-V photovoltaics." *Scientific Reports*, vol. 3, 2013.

[11] M. Woodhouse and A. Goodrich, "Manufacturing cost analysis relevant to single- and dual-junction photovoltaic cells fabricated with III-Vs and III-Vs grown on czochralski silicon (presentation)," National Renewable Energy Laboratory (NREL), Golden, CO., Tech. Rep., 2014.

[12] G. A. Landis and D. Hyatt, "The solar spectrum on the martian surface and its effect on photovoltaic performance," in *2006 IEEE 4th World Conference on Photovoltaic Energy Conference*, vol. 2. IEEE, 2006, pp. 1979–1982.

[13] M. S. Leite, R. L. Woo, J. N. Munday, W. D. Hong, S. Mesropian, D. C. Law, and H. A. Atwater, "Towards an optimized all lattice-matched InAlAs/InGaAsP/InGaAs multijunction solar cell with efficiency $> 50\%$," *Applied Physics Letters*, vol. 102, no. 3, 2013.

[14] Y. Rosenwaks, Y. Shapira, and D. Huppert, "Evidence for low intrinsic surface-recombination velocity on p-type InP," *Phys. Rev. B*, vol. 44, pp. 13 097–13 100, Dec 1991.

[15] S. M. Sze and M.-K. Lee, *Semiconductor Devices: Physics and Technology, 3rd Edition*, 3rd ed. John Wiley & Sons, May 2012.

[16] G. B. Stringfellow, G. B. Stringfellow, Ed. San Diego: Academic Press, 1999.

[17] R. S. Wagner and W. C. Ellis, "Vapor-Liquid-Solid Mechanism of Single Crystal Growth," *Applied Physics Letters*, vol. 4, no. 5, pp. 89–90, 1964.

[18] B. D. Cullity and S. R. Stock, *Elements of X-ray Diffraction*. Prentice Hall, 2001.

[19] S. Perkowitz, *Optical Characterization of Semiconductors Infrared, Raman, and Photoluminescence Spectroscopy*, ser. Techniques of physics ; 14. London ; San Diego: Academic Press, 1993.

[20] G. Perna, V. Capozzi, V. Augelli, T. Ligonzo, L. Schiavulli, G. Bruno, M. Losurdo, P. Capezzuto, J. L. Staehli, and M. Pallara, "Luminescence study of the disorder in polycrystalline inp thin films," *Semiconductor Science and Technology*, vol. 16, no. 5, p. 377.

VITA

Sean J. Babcock
Department of Electrical and Computer Engineering
Old Dominion University
Norfolk, VA 23529

Education

2015	Bachelor of Science	Electrical Engineering	Old Dominion University
2015	Bachelor of Science	Physics	Old Dominion University
2012	Associate of Science	Engineering	Tidewater Community College

Conference Proceedings

- Virtual Substrates for Low-Cost High Efficiency III-V Photovoltaics, S.J. Babcock, M.L. Lichty, G. Rajan, S. Marsillac, S.M. Hubbard, and C. G. Bailey, *44th IEEE Photovoltaic Specialists Conference*, June 2017, Washington, D.C.
- Thin-Film VLS Virtual Substrates for Low-Cost High Efficiency III-V Photovoltaics, S.J. Babcock, M.L. Lichty, S. Karki, G. Rajan, S. Marsillac, Z.S. Bittner, S.M. Hubbard, and C.G. Bailey, NASAs *24th Space Photovoltaic Research and Technology Conference*, September 2016, Cleveland, OH
- Phosphorization-Synthesized Virtual Substrates for Low-Cost High Efficiency III-V Photovoltaics, S.J. Babcock, M.L. Lichty, S. Karki, G. Rajan, S. Marsillac, Z.S. Bittner, S.M. Hubbard, J.S. McNatt, and C G. Bailey, *43rd IEEE Photovoltaic Specialists Conference*, June 2016, Portland, OR

Honors, Awards, Scholarships

- Graduate Student Service Award, Department of Electrical and Computer Engineering, Old Dominion University, 2017
- Solar Engineering Academic Program (SoLEAP) Scholarship, National Science Foundation, Award# 1355678, 2015-2017